2013

Optimal estimation for global ground-level fine particulate matter concentrations

Aaron van Donkelaar
Dalhousie University, Halifax, Nova Scotia, Canada

Randall V. Martin
Harvard-Smithsonian Center for Astrophysics, randall.martin@dal.ca

Robert J. D. Spurr
RT Solutions Inc., Cambridge, Massachusetts

Eason Drury
National Renewable Energy Laboratory, Golden,

Lorraine A. Remer
University of Maryland

See next page for additional authors

Authors
Aaron van Donkelaar, Randall V. Martin, Robert J. D. Spurr, Eason Drury, Lorraine A. Remer, Robert C. Levy, and Jun Wang

Optimal estimation for global ground-level fine particulate matter concentrations

Aaron van Donkelaar,[1] Randall V. Martin,[1,2] Robert J. D. Spurr,[3] Easan Drury,[4] Lorraine A. Remer,[5] Robert C. Levy,[6,7] and Jun Wang[8]

Received 14 February 2013; revised 3 May 2013; accepted 7 May 2013; published 10 June 2013.

[1] We develop an optimal estimation (OE) algorithm based on top-of-atmosphere reflectances observed by the MODIS satellite instrument to retrieve near-surface fine particulate matter ($PM_{2.5}$). The GEOS-Chem chemical transport model is used to provide prior information for the Aerosol Optical Depth (AOD) retrieval and to relate total column AOD to $PM_{2.5}$. We adjust the shape of the GEOS-Chem relative vertical extinction profiles by comparison with lidar retrievals from the CALIOP satellite instrument. Surface reflectance relationships used in the OE algorithm are indexed by land type. Error quantities needed for this OE algorithm are inferred by comparison with AOD observations taken by a worldwide network of sun photometers (AERONET) and extended globally based upon aerosol speciation and cross correlation for simulated values, and upon land type for observational values. Significant agreement in $PM_{2.5}$ is found over North America for 2005 (slope = 0.89; $r = 0.82$; 1-σ error = 1 μg/m^3 + 27%), with improved coverage and correlation relative to previous work for the same region and time period, although certain subregions, such as the San Joaquin Valley of California are better represented by previous estimates. Independently derived error estimates of the OE $PM_{2.5}$ values at in situ locations over North America (of ±(2.5 μg/m^3 + 31%) and Europe of ±(3.5 μg/m^3 + 30%) are corroborated by comparison with in situ observations, although globally (error estimates of ±(3.0 μg/m^3 + 35%), may be underestimated. Global population-weighted $PM_{2.5}$ at 50% relative humidity is estimated as 27.8 μg/m^3 at 0.1° × 0.1° resolution.

Citation: van Donkelaar, A., R. V. Martin, R. J. D. Spurr, E. Drury, L. A. Remer, R. C. Levy, and J. Wang (2013), Optimal estimation for global ground-level fine particulate matter concentrations, *J. Geophys. Res. Atmos.*, *118*, 5621–5636, doi:10.1002/jgrd.50479.

1. Introduction

[2] Long-term exposure to fine particulate matter with aerodynamic diameter less than 2.5 μm ($PM_{2.5}$) is associated with negative human health impacts, such as enhanced morbidity and mortality rates [*Dockery et al.*, 1993; *Pope et al.*, 2009]. Satellite-derived estimates of $PM_{2.5}$ are increasingly being incorporated into epidemiological studies [e.g., *Villeneuve et al.*, 2011; *Anderson et al.*, 2012; *Crouse et al.*, 2012] and more broadly into health impact assessments [*Lim et al.*, 2012]. A major strength of these satellite estimates is global coverage; this allows $PM_{2.5}$ exposure to be evaluated in locations without nearby in situ monitors. However, additional attention is needed to improving the accuracy and precision of satellite-derived estimates of $PM_{2.5}$.

[3] Top-of-atmosphere (TOA) reflectance (ρ_{TOA}) observed by passive satellite instrumentation such as the Moderate Resolution Imaging Spectroradiometer (MODIS) [*Levy et al.*, 2007b] is affected by molecular (Rayleigh) scattering, by surface reflectance, and by the total columnar extinction due to the presence of aerosol, known as the Aerosol Optical Depth (AOD). Satellite observations of ρ_{TOA} are often used to retrieve AOD using radiative transfer calculations. Retrieval accuracy is dependent upon input parameter uncertainties, of which surface reflectance dominates under low aerosol loading conditions and aerosol optical properties dominate at high aerosol loading conditions. The operational MODIS retrieval algorithm assigns aerosol optical properties according to location and season, and estimates surface reflectance using the MODIS 2.12 μm channel, at which the atmosphere is nearly transparent to fine aerosol [*Levy et al.*, 2007b]. Radiative

[1]Department of Physics and Atmospheric Science, Dalhousie University, Halifax, Nova Scotia, Canada.
[2]Harvard-Smithsonian Center for Astrophysics, Cambridge, Massachusetts, USA.
[3]RT Solutions Inc., Cambridge, Massachusetts, USA.
[4]National Renewable Energy Laboratory, Golden, Colorado, USA.
[5]JCET, University of Maryland, Baltimore, Maryland, USA.
[6]Science Systems and Applications, Inc. Lanham, Greenbelt, Maryland, USA.
[7]Earth Science Division, NASA Goddard Space Flight Center, Greenbelt, Maryland, USA.
[8]Department of Earth and Atmospheric Sciences, University of Nebraska-Lincoln, Lincoln, Nebraska, USA.

Corresponding author: A. van Donkelaar, Dalhousie University, 6300 Coburg Road, Halifax, NS, B3H 3J5, Canada. (Aaron.van.Donkelaar@dal.ca)

2169-897X/13/10.1002/jgrd.50479

transfer (RT) models can also be used to calculate the aerosol optical and land-surface properties that best match observations, allowing for modified retrieval algorithms [*Drury et al*., 2010; *Wang et al*., 2010].

[4] Passive nadir satellite observations, however, provide little information about the vertical extinction profile and about the relationship between extinction and mass. As a result, satellite-derived estimates of $PM_{2.5}$ require a conversion factor to relate retrieved AOD to $PM_{2.5}$; this factor must account for the local aerosol optical properties and the aerosol vertical profile, both of which are temporally and spatially variable. This conversion factor can be calculated through various empirical techniques [e.g., *Zhang et al*., 2009; *Kloog et al*., 2011] or by means of a chemical transport model (CTM) [e.g., *Liu et al*., 2004; *van Donkelaar et al*., 2011]. The inference of $PM_{2.5}$ from satellite observations can benefit from using consistent aerosol optical properties in both the AOD retrieval and in the conversion of AOD to $PM_{2.5}$ [*Drury et al*., 2010].

[5] CTMs solve for the temporal and spatial evolution of aerosol using meteorological data sets, emissions inventories, and equations that represent the physical and chemical behavior of atmospheric constituents. CTMs offer estimates of AOD and $PM_{2.5}$ that are largely independent from many of the error sources affecting satellite retrievals, such as surface reflectivity, but are dependent upon the accuracy of input parameters such as emissions and meteorology.

[6] *Van Donkelaar et al*. [2010] produced global $0.1^\circ \times 0.1^\circ$ satellite-derived $PM_{2.5}$ estimates that combined AOD from the Terra-satellite based MODIS and Multiangle Imaging Spectroradiometer [*Diner et al*., 1998] instruments with CTM-simulated AOD-$PM_{2.5}$ relationships, and found promising long-term mean agreement with in situ monitors over North America ($r = 0.77$, slope = 1.07) and globally ($r = 0.83$, slope = 0.86). Six years of $PM_{2.5}$ estimates were averaged to reduce the impact of random error. Surface reflectance-based filters were used to reduce systematic errors in the operational satellite retrievals, but these filters also reduced sampling in some regions.

[7] In this paper, we improve on these previous global estimates of $PM_{2.5}$ by developing an optimal estimation (OE) framework that combines satellite observations of ρ_{TOA} with a CTM based upon the local relative uncertainties of $PM_{2.5}$ derived from each source. OE is currently used for trace gas retrievals from several satellite instruments, including the Tropospheric Emission Spectrometer [*Bowman et al*., 2006], and has been demonstrated to be effective for the retrieval of aerosol properties [*Hasekamp and Landgraf*, 2005; *Waquet et al*., 2009; *Dubovik et al*., 2011]. It is also used by the Oxford-RAL Aerosols and Clouds retrieval from the Advanced Along Track Scanning Radiometer instrument [*Sayer et al*., 2012]. OE using ρ_{TOA} allows consistent optical properties to be used for both the AOD retrieval and calculation of the AOD to $PM_{2.5}$ conversion factors.

[8] Section 2 describes our algorithm, outlining our OE approach, the GEOS-Chem CTM, the Linearized Discrete Ordinate Radiative Transfer (LIDORT) RT model, and the data sources (MODIS, Aerosol Robotic Network (AERONET), and in situ $PM_{2.5}$). Section 3 describes our representation of surface reflectance, prior and observational error as incorporated into the OE framework, and evaluates the resulting AOD with AERONET measurements. Section 4 provides a detailed analysis of the simulated relative vertical aerosol profile using the space-borne Cloud-Aerosol Lidar with Orthogonal Polarization (CALIOP) lidar. Section 5 validates our final OE-based $PM_{2.5}$ values with available $PM_{2.5}$ measurements.

2. Approach and Data Sources

2.1. Optimal Estimation

[9] Optimal estimation (OE) provides a mathematical framework to combine observations and prior, or initial, estimates, based upon the theoretical relationship between simulated observations and retrieval quantities and the relative uncertainties of those observations, relationships, and prior estimates [*Rodgers*, 2000]. Vectors (denoted as bold) of observed values $\mathbf{y}$, treated as linearly related to retrieval quantities, are combined with prior estimates $\mathbf{x_a}$ to produce an optimal solution $\hat{\mathbf{x}}$,

$$\hat{\mathbf{x}} = \mathbf{x_a} + \mathbf{G}(\mathbf{y} - \mathbf{K}\mathbf{x_a}) \tag{1}$$

using the Jacobian, $\mathbf{K} = \frac{\partial \mathbf{y}}{\partial \mathbf{x}}$. The gain matrix, $\mathbf{G} = \mathbf{S_a}\mathbf{K}^{\mathrm{T}}(\mathbf{K}\mathbf{S_a}\mathbf{K}^{\mathrm{T}} + \mathbf{S_\varepsilon})^{-1}$, describes the sensitivity of the optimal solution to observation, based upon error in the prior $\mathbf{S_a}$ and observational $\mathbf{S_\varepsilon}$ values.

[10] For our optimal estimation, $\mathbf{y}$ is provided by ρ_{TOA} at two wavelengths from MODIS (section 2.4). AOD from the GEOS-Chem chemical transport model (section 2.2) is used to provide $\mathbf{x_a}$. The LIDORT radiative transfer model (section 2.3) is used to calculate $\mathbf{K}$. Sections 3.2 and 3.3 discuss determination of $\mathbf{S_a}$ and $\mathbf{S_\varepsilon}$.

[11] For linear inversion with Gaussian statistics (assumed in this work), the retrieved optimal estimate occurs at the minimum of the scalar-valued cost function $J(\mathrm{x})$:

$$J(\mathbf{x}) = (\mathbf{x} - \mathbf{x_a})^{\mathrm{T}}\mathbf{S_a}^{-1}(\mathbf{x} - \mathbf{x_a}) + (\mathbf{y} - \mathbf{K}\mathbf{x})^{\mathrm{T}}\mathbf{S_\varepsilon}^{-1}(\mathbf{y} - \mathbf{K}\mathbf{x}) \tag{2}$$

[12] This minimum of the inverse error-weighted difference of the solution and observed with prior values can be found analytically. In the case of a nonlinear forward-model relationship, such as that between TOA reflectance and AOD, the OE algorithm proceeds iteratively through a sequence of linear inversion problems until convergence is reached (relative change in optimal estimates between iterations is less than a pre-specified small quantity).

[13] The averaging kernel matrix $\mathbf{A}$ represents the sensitivity of final solution $\hat{\mathbf{x}}$ to the true value:

$$\mathbf{A} = \mathbf{G}\mathbf{K} \tag{3}$$

[14] The degrees of freedom for signal (DFS) is defined as the trace of $\mathbf{A}$ and denotes the number of independent pieces of information available in an observing system. Increased DFS indicates a decreased dependence on prior values and a more observationally constrained retrieval.

2.2. GEOS-Chem

[15] We use the GEOS-Chem Chemical Transport Model (http://geos-chem.org) to provide prior estimates of aerosol optical properties, AOD, and the AOD/$PM_{2.5}$ relationship using simulated aerosol throughout the entire atmospheric column and those simulated within the lowest grid box. The GEOS-Chem aerosol simulation (v8-03-01) includes

the sulphate-ammonium-nitrate-water system [*Park et al*., 2004], primary carbonaceous aerosols [*Park et al*., 2003], secondary organic aerosols [*Henze et al*., 2008], sea salt [*Alexander et al*., 2005], and mineral dust [*Fairlie et al*., 2007]. Gas-aerosol equilibrium is computed using ISORROPIA II [*Pye et al*., 2009]. The aerosol and oxidant simulations are coupled through formation of sulphate and nitrate [*Park et al*., 2004], heterogeneous chemistry [*Jacob*, 2000; *Evans and Jacob*, 2005; *Thornton et al*., 2008], and aerosol effects on photolysis rates [*Martin et al*., 2003b; *Lee et al*., 2009].

[16] Our global GEOS-Chem simulation uses assimilated meteorology from the Goddard Earth Observing System (GEOS-5), degraded to $2^\circ \times 2.5^\circ$ horizontal resolution and 47 vertical levels. The GEOS-Chem nested capability uses the native $1/2^\circ \times 2/3^\circ$ GEOS-5 resolution over regions of North America, Europe, and Asia [*Chen et al*., 2009; *van Donkelaar et al*., 2012]. Nested simulation results are used whenever a retrieval pixel falls within a nested domain.

[17] Global anthropogenic emissions are based upon EDGAR 3.2FT2000 [*Olivier et al*., 2002]. Global anthropogenic emissions are overwritten in areas with regional inventories, including NEI05 (United States; http://www.epa.gov/ttnchie1/net/2005inventory.html), CAC05 (Canada; http://www.ec.gc.ca/inrp-npri/), EMEP (Europe; http://www.emep.int/), BRAVO (Mexico) [*Kuhns et al*., 2005], and for East Asia [*Streets et al*., 2003; *Streets et al*., 2006]. Inventories are scaled from their base year up to a maximum of 2007, as described in *van Donkelaar et al*. [2008]. Eight day GFED2 emissions are used for biomass burning [*Nassar et al*., 2009].

2.3. LIDORT

[18] We simulate ρ_{TOA} using the Linearized Discrete Ordinate Radiative Transfer (LIDORT) radiative transfer model (version 3.4) [*Spurr*, 2008]. AOD Jacobians (partial derivatives of ρ_{TOA} with respect to AOD) may also be generated analytically from this RT model. LIDORT uses the discrete ordinate method to solve the RT equation in each layer, plus a linear boundary value technique to determine the whole-atmosphere radiation field. LIDORT uses the pseudo-spherical approximation (solar beam attenuation in a curved atmosphere before plane-parallel scattering). The model requires pre-computed inputs of vertically resolved atmospheric extinction, single scattering albedo, and phase function Legendre expansion coefficients. These aerosol optical properties are obtained from tabulated output from Mie simulations [*de Rooij and van der Stap*, 1984; *Mishchenko et al*., 1999] following *Martin et al*. [2003a] with 64 moments and applied to GEOS-Chem relative humidity dependent fields, sampled coincidently with MODIS observations. T-matrix calculations were used to represent nonspherical effects of dust [*Wang et al*., 2003]. Other inputs are surface reflectance, solar zenith angle, and viewing zenith angle. Surface reflectance is described in section 3.1.

2.4. MODIS

[19] Two MODIS instruments presently orbit the Earth onboard the Aqua and Terra satellites, with respective daytime equator-crossing times of 10:30 A.M. and 1:30 P.M. Each MODIS instrument provides near-daily global observation at 36 wavelength bands, seven of which were specifically designed for aerosol retrieval. The operational AOD product from both MODIS instruments (MOD/MYD04) provides global retrievals over dark surfaces free of snow, ice, and cloud at a nadir resolution of 10 km × 10 km with an accuracy of $\pm(0.05 + 15\%)$ [*Levy et al*., 2007b]. The retrieval algorithm assumes minimal optical influence of atmospheric aerosol and gases at the 2.12 μm band and retrieves the 2.12 μm surface reflectance ($\rho_{\mathrm{s,2.12\,\mu m}}$) during the inversion procedure that uses TOA reflectances at 0.47 μm, 0.66 μm, and 2.12 μm as input. $\rho_{\mathrm{s,2.12\,\mu m}}$ is related to surface reflectance at the aerosol retrieval wavelengths of 0.47 μm ($\rho_{\mathrm{s,0.47\,\mu m}}$) and 0.66 μm ($\rho_{\mathrm{s,0.66\,\mu m}}$) using globally fixed relationships dependent on values of the Normalized Difference Vegetation Index constructed from the shortwave infrared (SWIR) bands at wavelengths 1.24 μm and 2.12 μm. These relationships are derived from a data base of atmospherically corrected MODIS reflectances at AERONET AOD observations and aerosol optical properties based on an AERONET climatology [*Levy et al*., 2007a]. This approach has proven to be globally effective, but regional bias does exist where local surface reflectance relationships vary from the assumed global norms [*Drury et al*., 2008; *Kahn et al*., 2009; *Levy et al*., 2010].

[20] For our OE observational input, we use ρ_{TOA} from Collection 5 MOD/MYD04; this has been screened for cloud and bright surfaces. We find that MODIS-Terra's globally averaged ρ_{TOA} decreases relative to MODIS-Aqua values by 0.24–0.35% per year between mid-2003 and 2009, depending on wavelength. This suggests a slight loss of MODIS-Terra's sensitivity as similar trends should be observed by both instruments. In order to ensure consistency across platforms, we scale the global annual average MODIS-Terra radiances for each wavelength to those observed from MODIS-Aqua before to incorporation into the OE framework. The recently available Collection 6 MODIS radiances should remove the need for such an adjustment in future retrievals [*Levy et al*., 2013; *Remer et al*., 2013].

2.5. AERONET

[21] The Aerosol Robotic Network (AERONET) is a globally distributed network of CIMEL Sun photometers [*Holben et al*., 1998] that provide multi-wavelength AOD measurements with a low uncertainty of < 0.02 [*Holben et al*., 2001]. AERONET provides an invaluable validation data set for AODs, whether simulated or retrieved from satellite observations. AERONET observations are used to derive surface reflectance properties (section 3.1), as well as prior (section 3.2) and observational uncertainties (section 3.3) for our MODIS AOD retrieval.

2.6. CALIOP

[22] The Cloud-Aerosol lidar with Orthogonal Polarization (CALIOP) instrument has provided global aerosol profiles from onboard the Cloud-Aerosol Lidar and Infrared Pathfinder Satellite Observation satellite since 2006 [*Winker et al*., 2009]. CALIOP observes the backscattered radiation from laser pulses it emits at 1064 nm and 532 nm and retrieves extinction profiles at a resolution of 30 m vertical and 335 m horizontal. The CALIOP retrieval relies on a knowledge of the local particulate extinction-to-backscatter ratio, known as the lidar ratio, S_p. Properties such as observed polarization and geographic location are used to predict aerosol type [*Omar et al*., 2009]. A lookup table is then typically

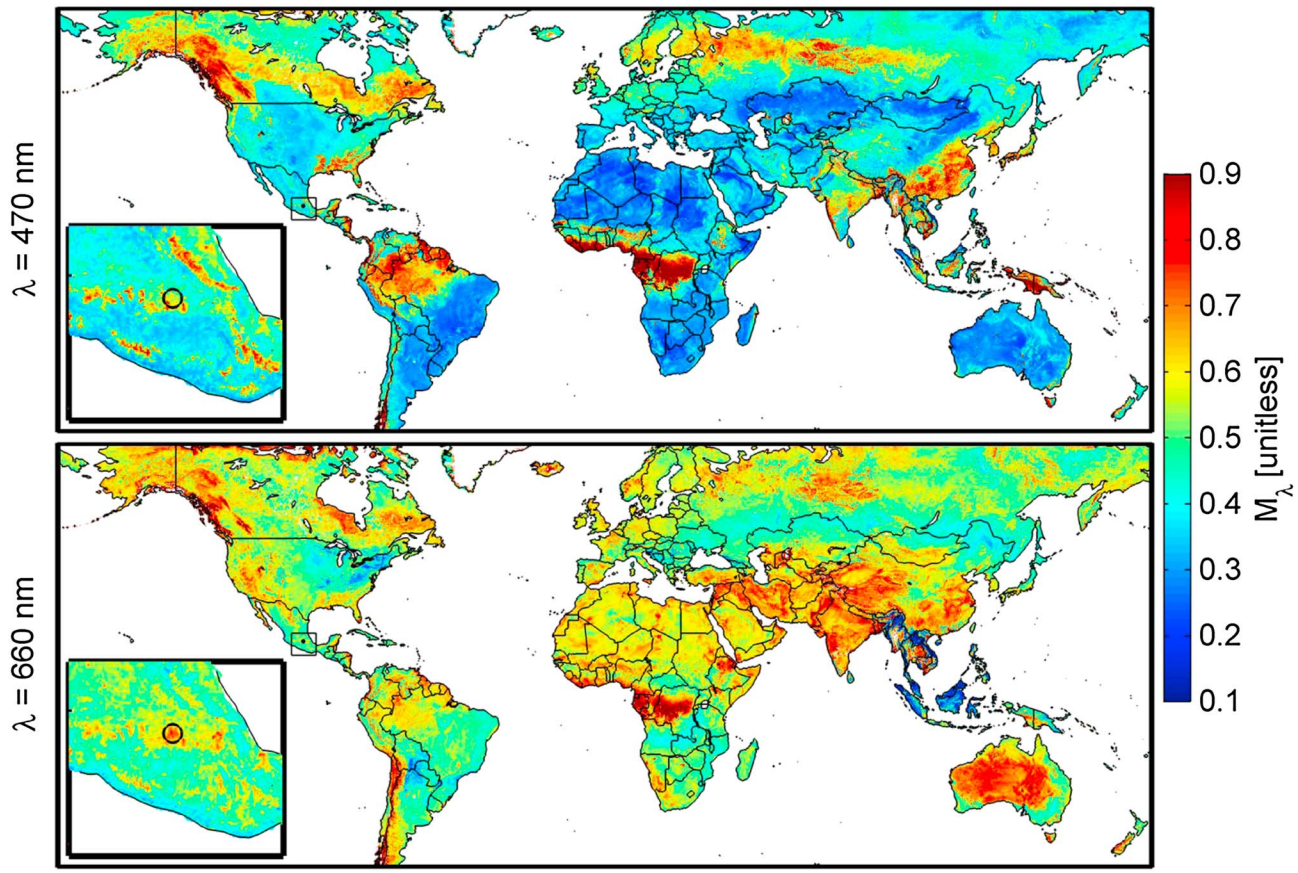

Figure 1. Ratio of isotropic surface reflectance components at wavelength λ to 2.12 μm (M_λ) for July 2008. The insets are enlargements of the Central American region identified on the global plot; the circle indicates the location of Mexico City.

used to determine the values of S_p from an observationally based data set. The impact of S_p on retrieved extinction profiles is discussed in section 4.

2.7. In Situ Observations

[23] Near-surface, in situ $PM_{2.5}$ measurements are used from a combination of the Canadian National Air Pollution Surveillance Network (NAPS; http://www.etc.cte.ec.gc.ca/NAPS/index_e.html), the Interagency Monitoring of Protected Visual Environments (http://vista.cira.colostate.edu/improve/Data/data.htm), and U.S. Environmental Protection Agency Air Quality System Federal Reference Method (http://www.epa.gov/air/data/index.html) sites. We additionally include the global values described in *van Donkelaar et al*. [2010], which use reported network data from Europe, Australia, New Zealand, and South America, as well as annually representative, published values from the literature throughout the rest of the world. This compilation of in situ $PM_{2.5}$ data is used to validate our final satellite-derived $PM_{2.5}$ estimates. We note that in situ $PM_{2.5}$ observations are collected at either 35% or 50% relative humidity, according to local national standards.

3. Optimal Estimation of Aerosol Optical Depth

[24] The OE algorithm in this work requires information on surface reflectance, along with a knowledge of the prior and observational errors. Each is discussed below. In brief, we use AERONET observations of AOD to develop a surface reflectance parameterization, as well as estimate prior and observational errors. A global analysis is performed using daily MODIS ρ_{TOA} at 10 km × 10 km for 2005.

3.1. Estimation of Surface Reflectance

[25] Coarse aerosols can affect the top-of-atmosphere reflectance in the near-IR [*Wang et al*., 2010]. We calculate the effect of these aerosols on $\rho_{TOA,2.12\,\mu m}$ using simulated aerosol fields from GEOS-Chem as input to LIDORT calculations of ρ_{TOA}. We simulate and remove the contribution of atmospheric aerosols from $\rho_{TOA,2.12\,\mu m}$ to estimate the surface value ($\rho_{s,2.12\,\mu m}$) and subsequently relate the isotropic component to the other wavelengths (λ) of 0.47 μm and 0.66 μm, assuming the following linear relationship:

$$\rho_{s,\lambda} = \upsilon_\lambda \left(\frac{M_\lambda}{\upsilon_{2.12\ \mu m}} \left(\rho_{TOA,2.12\ \mu m} - \left(\rho_{TOA,2.12\ \mu m} - \rho_{TOA,2.12\ \mu m}^{NO\ AEROSOL} \right)_{sim} \right) + B_\lambda \right) \quad (4)$$

where $\rho_{TOA,2.12\ \mu m,sim}$ and $\rho_{TOA,2.12\ \mu m,sim}^{NO\ AEROSOL}$ are simulated ρ_{TOA} at 2.12 μm with and without aerosol present. υ_λ and $\upsilon_{2.12\ \mu m}$ are the ratios of isotropic and Ross-Li (isotropic + volumetric + geometric) surface reflectance at wavelengths λ and 2.12 μm as inferred from a monthly mean of the MODIS

Table 1. Median and Standard Deviation of Isotropic Surface Reflectance Ratios (M_λ) at 470 nm and 660 nm With Isotropic Surface Reflectance at 2.12 μm, Median Degrees of Freedom of Signal (DFS) and Relative Weight for Observational Constraint (Obs. Weight)

	470 nm			660 nm				
Land Cover Type	MOD04	MOD43	This Work	MOD04	MOD43	This Work	DFS	Obs. Weight[a]
Evergreen needleleaf forest	0.29 ± 0.02	0.42 ± 0.12	0.62 ± 0.11	0.58 ± 0.04	0.62 ± 0.09	0.57 ± 0.09	0.46	35:65
Evergreen broadleaf forest	0.30 ± 0.01	0.57 ± 0.25	0.68 ± 0.25	0.60 ± 0.02	0.65 ± 0.17	0.57 ± 0.22	0.57	4:96
Deciduous needleleaf forest	0.30 ± 0.02	0.34 ± 0.05	0.46 ± 0.05	0.60 ± 0.02	0.53 ± 0.04	0.51 ± 0.04	0.34	2:98
Deciduous broadleaf forest	0.30 ± 0.02	0.30 ± 0.11	0.36 ± 0.13	0.61 ± 0.05	0.49 ± 0.07	0.30 ± 0.09	0.55	41:59
Mixed forests	0.29 ± 0.01	0.43 ± 0.11	0.53 ± 0.10	0.61 ± 0.01	0.56 ± 0.07	0.50 ± 0.08	0.67	11:89
Closed shrublands	0.24 ± 0.03	0.30 ± 0.17	0.36 ± 0.17	0.49 ± 0.05	0.58 ± 0.17	0.54 ± 0.17	0.24	17:83
Open shrublands	0.25 ± 0.03	0.33 ± 0.09	0.40 ± 0.10	0.51 ± 0.05	0.61 ± 0.09	0.61 ± 0.10	0.29	77:23
Woody savannas	0.29 ± 0.03	0.36 ± 0.11	0.42 ± 0.16	0.59 ± 0.05	0.58 ± 0.08	0.51 ± 0.10	0.47	71:29
Savannas	0.26 ± 0.02	0.26 ± 0.05	0.31 ± 0.05	0.53 ± 0.05	0.53 ± 0.05	0.51 ± 0.06	0.45	46:54
Grasslands	0.24 ± 0.02	0.29 ± 0.07	0.30 ± 0.07	0.49 ± 0.04	0.58 ± 0.09	0.54 ± 0.08	0.18	99:1
Permanent wetlands	0.28 ± 0.01	0.44 ± 0.16	0.81 ± 0.22	0.57 ± 0.02	0.75 ± 0.15	0.75 ± 0.15	0.32	46:54
Croplands	0.28 ± 0.02	0.30 ± 0.10	0.38 ± 0.12	0.58 ± 0.04	0.55 ± 0.13	0.51 ± 0.14	0.53	90:10
Urban and built-up	0.27 ± 0.02	0.37 ± 0.10	0.51 ± 0.12	0.55 ± 0.04	0.66 ± 0.11	0.64 ± 0.11	0.43	69:31
Cropland/natural vegetation mosaic	0.29 ± 0.01	0.33 ± 0.11	0.45 ± 0.18	0.60 ± 0.03	0.56 ± 0.12	0.55 ± 0.15	0.55	29:71
Barren or sparsely vegetated	0.25 ± 0.01	0.30 ± 0.13	0.32 ± 0.13	0.50 ± 0.01	0.68 ± 0.13	0.61 ± 0.13	0.20	97:3

[a]Defined as the ratio of median percentage error of M_{660} and median percentage of M_{470}, normalized to 100.

BRDF product (MOD43 V5) [*Lucht et al*., 2000]; these ratios account for the effect of solar and viewing geometry on $\rho_{s,\lambda}$. M_λ, and B_λ are the ratio and offset between the isotropic components of $\rho_{s,\lambda}$ and $\rho_{s,2.12\ \mu m}$. We initialize M_λ as the monthly mean isotropic surface reflectance ratio from MOD43, and initially set B_λ to zero.

[26] The global collection of AERONET AOD measurements encompass a variety of land types and provide an opportunity to evaluate and improve these surface reflectance estimates. We calculate AOD at 550 nm from ρ_{TOA} at each wavelength, increasing the prior error ($\mathbf{S_a} \rightarrow \infty$) to remove the influence of the prior. In addition to the MOD/MYD04 filters, we use the snow-cover estimates from MOD43 to remove any areas that have detected snow within a 16 day window.

[27] We compare AERONET AOD ($\tau_{AERONET}$) with these individual MODIS AOD (τ_{MODIS}) values that are within a surrounding square of 5×5 pixels (approximately 50 km 50 km) around each AERONET station and interpret their difference to reduce bias in surface reflectance:

$$\Delta\rho_{s,\lambda} = \frac{\partial \rho_{s,\lambda}}{\partial \tau}(\tau_{MODIS} - \tau_{AERONET}) \quad (5)$$

where $\Delta\rho_{s,\lambda}$ is the change in $\rho_{s,\lambda}$ equivalent to the difference between observed and retrieved AOD. The derivative $\frac{\partial \rho_{s,\lambda}}{\partial \tau}$ is determined from LIDORT. This approach assumes that differences in AOD are strictly the result of surface reflectance error. Error in the assumed aerosol microphysical properties would also play a role and, if large, may compromise this approach.

[28] This AOD comparison was carried out for the 5 year period 2004–2008. We investigate variability of $\Delta\rho_{s,\lambda}$ as a function of $\rho_{s,2.12\ \mu m}$, month, and land cover type as defined by the MODIS land cover product (MOD12C1) [*Freidl et al*., 2010]. We group AERONET stations within continuous land type regions, defined by 5% contours of each land type percent coverage, and determine the changes to M_λ and B_λ (ΔM_λ and ΔB_λ) needed to reduce bias between the calculated and observed AOD.

[29] We predict ΔM_λ and ΔB_λ for each land type region based upon the inverse AOD-weighted median of the highest decile of observed land type fraction. This method infers the characteristics of each surface type over locations dominated by that surface type. Regions with less than 50% land type coverage are excluded from the prediction of ΔM_λ and ΔB_λ. We assume that changes determined for the surface reflectance relationship of each land cover type at AERONET locations are representative over large distances and use an inverse distance weighted spatial interpolation to extend the land type-specific ΔM_λ and ΔB_λ values to regions without collocated AERONET observations. Average ΔM_λ and ΔB_λ, weighted by percent land type coverage, are superimposed onto the relationships calculated from the MODIS BRDF product and maintain its initial fine scale variability. This process is iterated, with each iteration capped at 80% of the previous change, until ΔM_λ is less than 0.01 of the previously estimated value.

[30] Figure 1 shows our final estimates of M_λ for July 2008. Red coloring denotes regions where surface reflectance at 470 nm and 660 nm approach that at 2.1 μm; this is characteristic of densely vegetated regions of low 2.1 μm surface reflectance such as in Brazil, the Congo, eastern Asia, and the southeast United States. At 660 nm, higher ratios are found in the western United States as compared to the eastern United States, principally due to bright, arid surfaces in the west. Surface reflectance over desert regions decrease by about a factor of 2 between 660 nm and 470 nm, a result similar to that found by *Hsu et al*. [2006].

[31] Table 1 gives the median and standard deviation of M_λ for July 2008 according to MOD/MYD04, MOD43, and this work. The MOD43 values used for initial surface reflectivity remain globally well correlated with our final estimates at $0.1^\circ \times 0.1^\circ$ for both wavelengths ($r = 0.92$ to 0.93). The correlation of our final M_λ with MOD/MYD04 values is low ($r = -0.2$ to 0.3) which show less variability within each land cover type. Our final values are generally higher than MOD/MYD04 at 470 nm, with a median difference of 0.14, but are globally more similar at 660 nm, with a median difference of 0.02. Some of these differences at 470 nm require further investigation in future work.

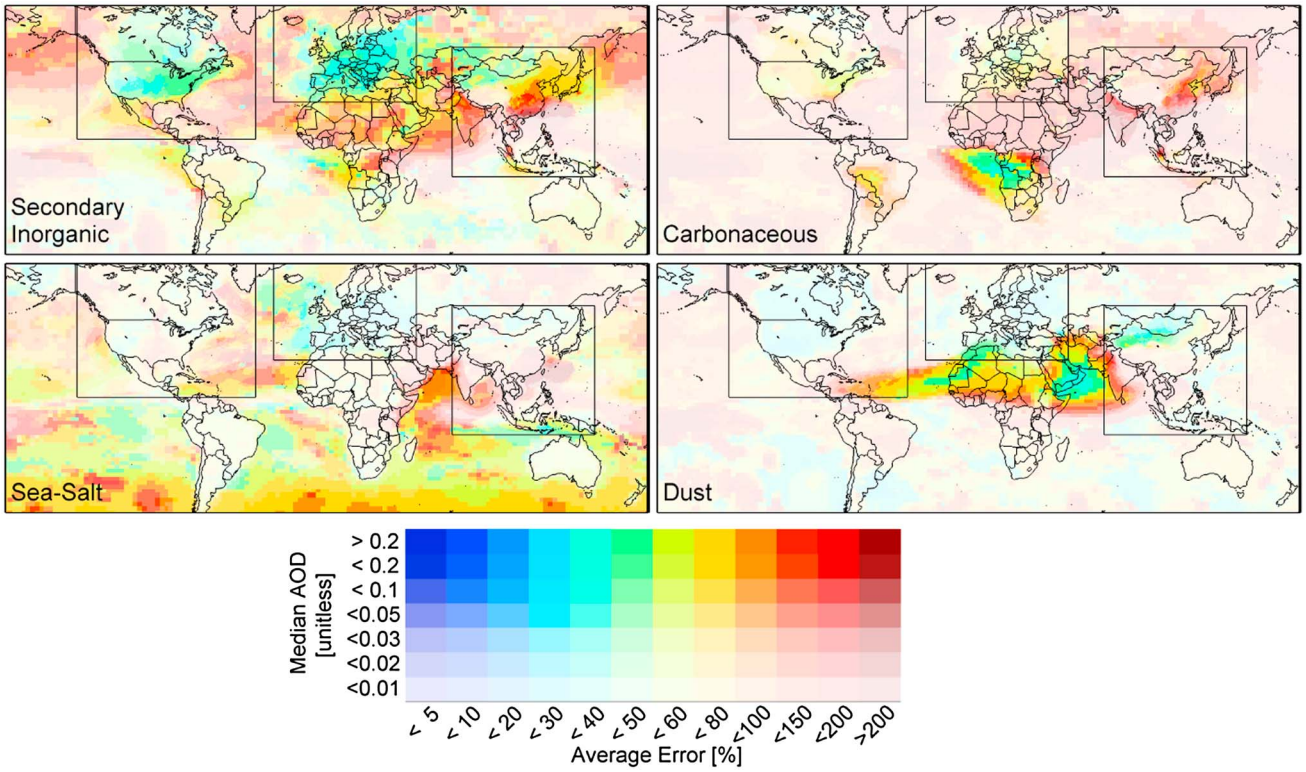

Figure 2. Average speciated error in prior Aerosol Optical Depth (AOD) at 550 nm for the month of July. Boxes indicate the domains of GEOS-Chem nested regions. Intensity of color represents the median speciated simulated AOD during July 2004–2008. Speciated groupings are named in the lower left corner of each panel.

[32] Transitions from vegetative surfaces to urban surfaces have the potential to cause errors in AOD retrievals, due to increased reflectance of urban surfaces [*de Almeida Castanho et al.*, 2007]. The insets in Figure 1 highlight such a transition in Mexico, where $M_{0.66\,\mu m}$ increases to 0.75 over Mexico City. *De Almeida Castanho et al.* [2007] determined that a visible/SWIR surface reflectance ratio for urban Mexico City of 0.73 significantly improved MODIS retrievals during the Megacity Initiative: Local and Global Research Observations campaign of March 2006, which is in agreement with our value during that time.

3.2. Estimation of Prior Error

[33] OE relies on an accurate representation of error for both the initial or prior quantities as well as observed quantities. We estimate the prior error by comparing GEOS-Chem AOD with daily coincident AERONET observations over 2004–2008 for each month. A knowledge of this error as a function of aerosol species is helpful in extending error estimates beyond AERONET locations, since species-specific emissions and assumed aerosol microphysical properties are major sources of CTM error. We estimate the role of different species in contributing to CTM error by applying the relative simulated speciation to AERONET AOD. The observations are subdivided by species (sulphate-ammonium-nitrate, carbonaceous, dust, and sea salt) and magnitude before comparison. We exclude speciated fractions below 20% and combine those stations within 1000 km. This regional grouping of

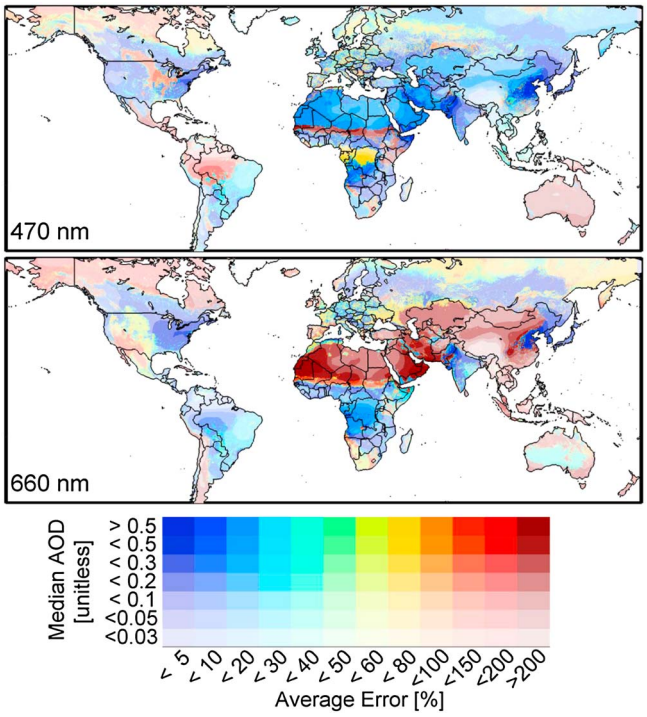

Figure 3. Average error in observational AOD for the month of July. Intensity of color represents the median speciated prior AOD during July 2004–2008. Observational wavelengths used to calculate AOD at 550 nm are given in the lower left corner of each panel.

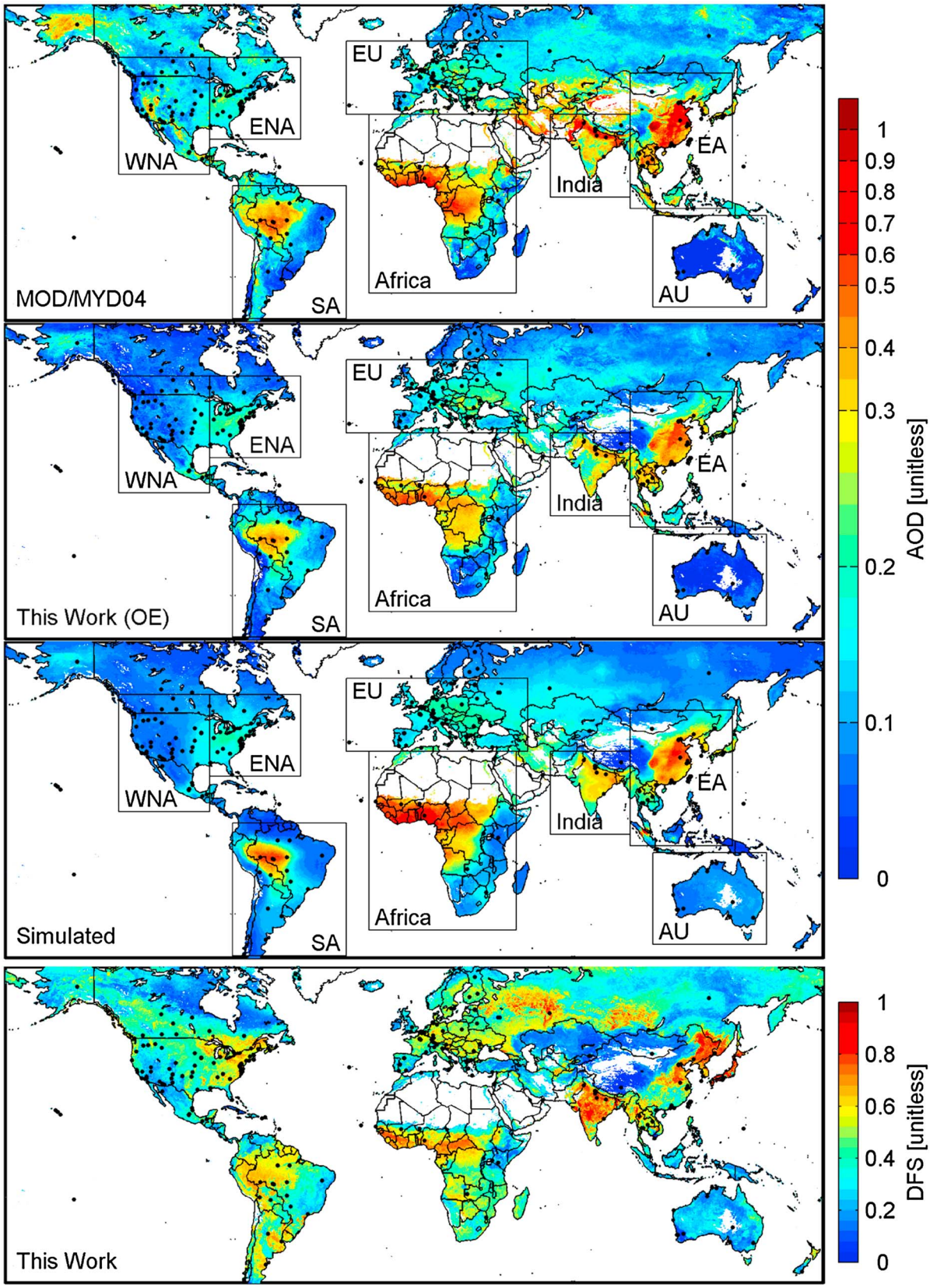

Figure 4. (top three panels) Average of coincidently sampled AOD at 550 nm from the operational MODIS retrieval (MOD/MYD04), from optimal estimation (this work), and from simulations (GEOS-Chem) for January to December 2005. (bottom panel) Degrees of freedom for signal (DFS) for the optimal estimation. Boxed regions denote those used for the scatterplots of Figure 5. Black dots indicate AERONET locations. White areas denote lack of data (less than 10 values) or water.

Table 2. Lidar Ratio at 532 nm Calculated With GEOS-Chem Aerosol Optical Properties, as a Function of Relative Humidity

Species	Relative Humidity (%)					
	0	50	70	80	90	95
Ammonium sulphate	54	66	71	75	83	90
Black carbon	108	108	108	96	80	73
Organic carbon	56	62	64	66	71	75
Sea salt (accumulation)	16	26	25	24	23	21
Sea salt (coarse)	14	15	18	19	19	19

AERONET stations is used to improve the number of comparisons available for each month and assumes a regionally similar magnitude of error for each species. We calculate the 1-σ percentage and absolute error of each species at each station as a function of magnitude. We extend these errors globally using an inverse distance and cross-correlation weighted average. Locations that lack statistically significant cross correlations are not included in the weighted average. Additionally, we use this comparison to determine a minimum overall error for simulated AOD using the absolute 1-σ error at low total AOD (<0.05).

[34] Figure 2 shows the average daily 1-σ percentage error in simulated AOD at 550 nm at overpass time by species for July. Errors of 40%–60% in secondary inorganic (sulphate, ammonium, and nitrate) AOD are found in most regions of North America and Europe, where these species can dominate AOD. Asian errors are typically higher for all species, particularly in India where errors exceed 100% for all dominant species (carbonaceous aerosol, secondary inorganic aerosol, and dust). Errors in dust are typically 30%–100% near major source regions but have limited influence elsewhere. The errors in sea salt have a limited effect on AOD over land, where sea-salt concentrations are low.

3.3. Estimation of Observational Error

[35] We use a "brute-force" technique to determine the observational accuracy at both 0.47 μm and 0.66 μm as a function of month, land cover type, and magnitude of AOD. This observational error term includes uncertainty in both the observed ρ_{TOA} and the retrieval skill at relating ρ_{TOA} to AOD at 550 nm and is impacted by local accuracies of the extinction profile, surface reflectivity, and aerosol microphysical properties. OE calculations are performed for MODIS footprints within the surrounding square of 5×5 pixels (approximately 50 km × 50 km) for each AERONET location using a series of assumed errors and then compared with AERONET. We separate comparison pairs according to land cover and combine stations following our approach for surface reflectance estimation.

[36] We determine the monthly absolute and percentage observational error of each land type by evaluation at each AERONET site using these land cover separated values. We evaluate local agreement by considering the four metrics slope (m), offset (b), root mean square difference (rmsd), and correlation coefficient (r) versus AERONET observations. We equally weight the importance of each metric, normalize the individual terms such that a value of 1 denotes its preferred condition, and then sum to create a ranking over the range 0 to 4, where we define this rank as:

$$\mathrm{rank} = \min(m, m^{-1}) + (1 - \mathrm{abs}(b)/b_{75}) + r + (1 - \mathrm{abs}(\mathrm{rmsd})/\mathrm{rmsd}_{75}) \quad (6)$$

[37] Negative terms are set to zero. Here b_{75} and rmsd_{75} denote the 75th percentile of their respective values, beyond which scores are set to zero for these metrics. An inverse distance weighted spatial interpolation is used to produce a global map of error for each land cover type. Finally, these land cover specific errors are combined based upon local percent land type coverage to create a global error map.

[38] Figure 3 shows the resulting average daily percentage error in AOD for July 2005 at both observational wavelengths. Errors at 470 nm tend to be less than 50%. Errors at 660 nm are more variable and exceed 100% over most deserts. Errors in observed AOD tend to be lower than in the simulated, prior, values with the exception of arid regions at 660 nm. Errors at 470 nm are typically lower than at 660 nm over the western United States and other bright surfaces; this is likely indicative of darker surfaces at 470 nm and the quality of surface reflectance relationships over these regions. Observational errors below 20% over some heavily polluted regions of India and China suggest that observational constraints may significantly improve upon prior AOD in these regions. We again determine a minimum overall error using the absolute 1-σ error at low AOD (<0.05).

[39] Table 1 gives the relative weight of each wavelength on the observational constraint, as implied by the normalized ratio of median percentage error at each wavelength. Forested regions are dominated by the 660 nm wavelength, suggesting a better surface characterization at this wavelength. Urban and cropland surfaces, by contrast, appear to be better represented by the 470 nm surface relationships. The implication of low DFS, also given in Table 1, for certain land cover types is discussed below.

3.4. Comparison of Operational, Simulated, and OE AOD

[40] Given the errors calculated in sections 3.2 and 3.3, we now proceed to calculate the optimal estimate by minimizing the cost function in equation 2. Figure 4 (top three panels) shows the average coincidently sampled AOD from the operational algorithm (MOD/MYD04), from our OE algorithm, and from simulation. Differences between OE and operational values result from the influence of the prior and from differences in assumed surface reflectance and aerosol optical properties. Strong AOD enhancements above global mean values are seen over eastern China and northern India, as well as biomass burning regions in Africa and South America. OE AOD over western North America does not show the same enhancement as seen in MOD/MYD04, consistent with *Drury et al.* [2008]. Higher correlation is

Table 3. CALIOP Aerosol Types and Associated Lidar Ratios at 532 nm [From *Winker et al.*, 2009]

Species	Lidar Ratio
Dust	40
Smoke	70
Clean continental	35
Polluted continental	70
Clean marine	20
Polluted dust	65

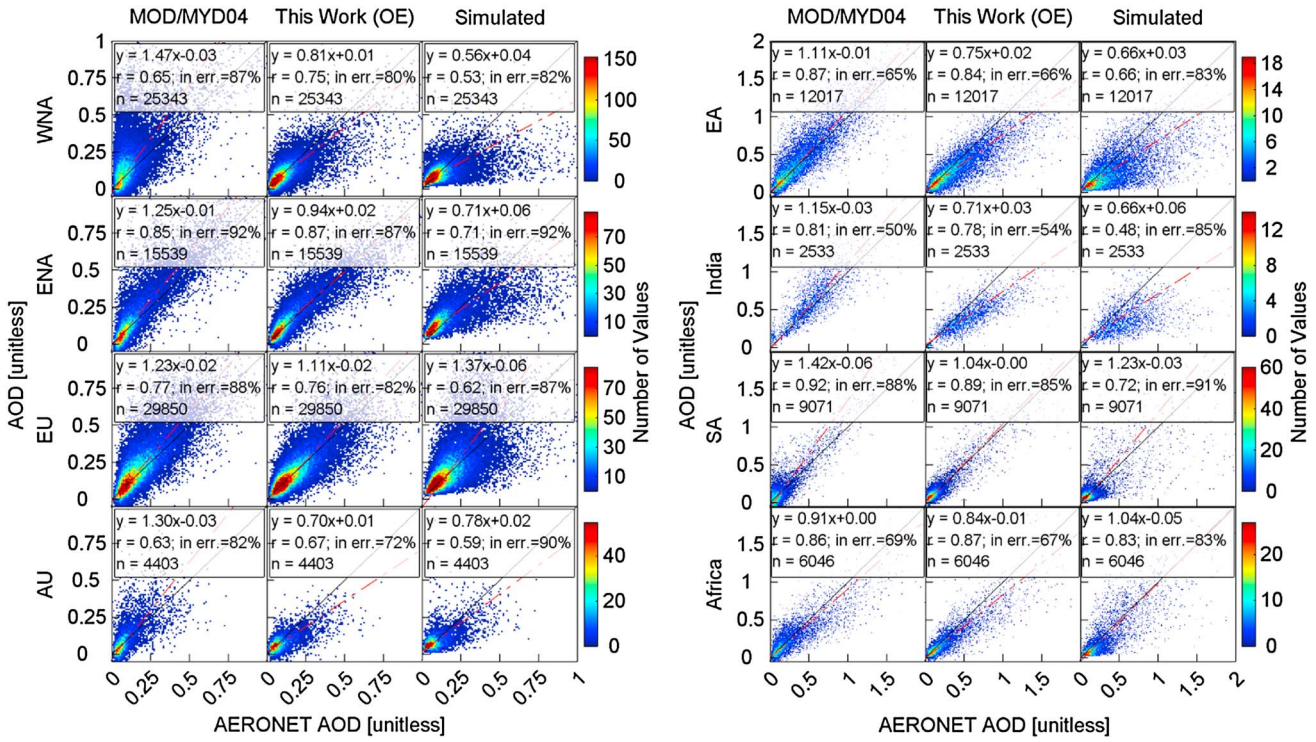

Figure 5. Scatterplots of coincident operational (MOD/MYD04), optimal estimation (this work), and simulated (GEOS-Chem) AODs compared against AERONET values at 550 nm. Simulated and optimal estimation error estimates are given in Figures 2 and 3. Regions are defined in Figure 4. In err. indicates the percentage of AOD pairs within the expected error bound of each dataset.

found between OE AOD and simulated values ($r = 0.86$) compared to MOD/MYD04 ($r = 0.72$) but both show significant agreement.

[41] The bottom panel of Figure 4 shows the average DFS, as calculated from the trace of the averaging kernel matrix. Values exceed 0.8 over India and eastern China, indicating a regionally high sensitivity to aerosol loading. DFS less than 0.5 over bright surfaces indicates a stronger dependence on the prior in regions such as the western United States and central Asia. Table 1 summarizes median DFS by land cover type. Low values (<0.25) are found over barren or sparsely vegetated, grassland, and closed shrubland surfaces, indicated a poor representation of surface reflectance at both wavelength for these land cover types. Forested land cover types typically show the greatest level of observational constraint (DFS = 0.34–0.67). Cropland-related land covers are also relatively constrained (DFS = 0.53–0.57).

[42] Figure 5 compares MOD/MYD04, OE, and simulated AOD with coincident observations from AERONET. OE correlations and slopes typically perform as well as, or better, than either MOD/MYD04 or simulation. The most prominent exceptions are for eastern Asia and India where MOD/MYD04 is biased high by 11–15%, while OE is biased low by 25–29%. These regions have high prior error and rely heavily on observational values, as represented by the high DFS. Brighter surface reflectance is assumed in this region by this work as compared to the MOD/MYD04 algorithm, however, and therefore, AOD is decreased. An increase in the density of AERONET observations in these regions would allow better characterization of regional surface properties. Africa shows a slight loss in performance (slope = 0.84) relative to the MOD/MYD04 retrieval (slope = 0.91), despite a slope of 1.04 for the prior. Further improvements to surface reflectance would help here.

[43] Figure 5 also contains the number of coincident pairs whose difference lie within the given error for each data set. We find that at least 68% (1-σ) of the operational, simulated, and OE error estimates are within the expected values of (15% + 0.05) for MOD/MYD04 [*Remer et al.*, 2005] and those given in Figures 1 and 2, with the exception of the Indian subcontinent, where operational and OE error estimates are underestimated. Local OE error envelopes typically capture fewer values as the slope deviates further from unity, suggesting that bias may be inadequately represented.

4. Effect of Relative Vertical Profile on $PM_{2.5}$

[44] Here we discuss the aerosol vertical profiles used to related total column AOD to ground-level concentrations. Satellite observations of ρ_{TOA} from a single nadir viewing geometry are unable to resolve information on the aerosol vertical profile needed to determine near-surface $PM_{2.5}$. We therefore rely on simulated vertical profile to relate total column AOD to $PM_{2.5}$. We evaluate the simulated relative profile using CALIOP. Following *Ford and Heald* [2012], we remove simulated values below the CALIOP detection limit, exclude cloud aerosol detection scores below 20, and limit total column optical depths to less than 2.0.

[45] Consistent aerosol optical properties in both the CALIOP retrieval and the aerosol simulation are necessary to isolate the information from CALIOP observations about bias in simulated profiles. Table 2 gives the lidar ratio, S_p,

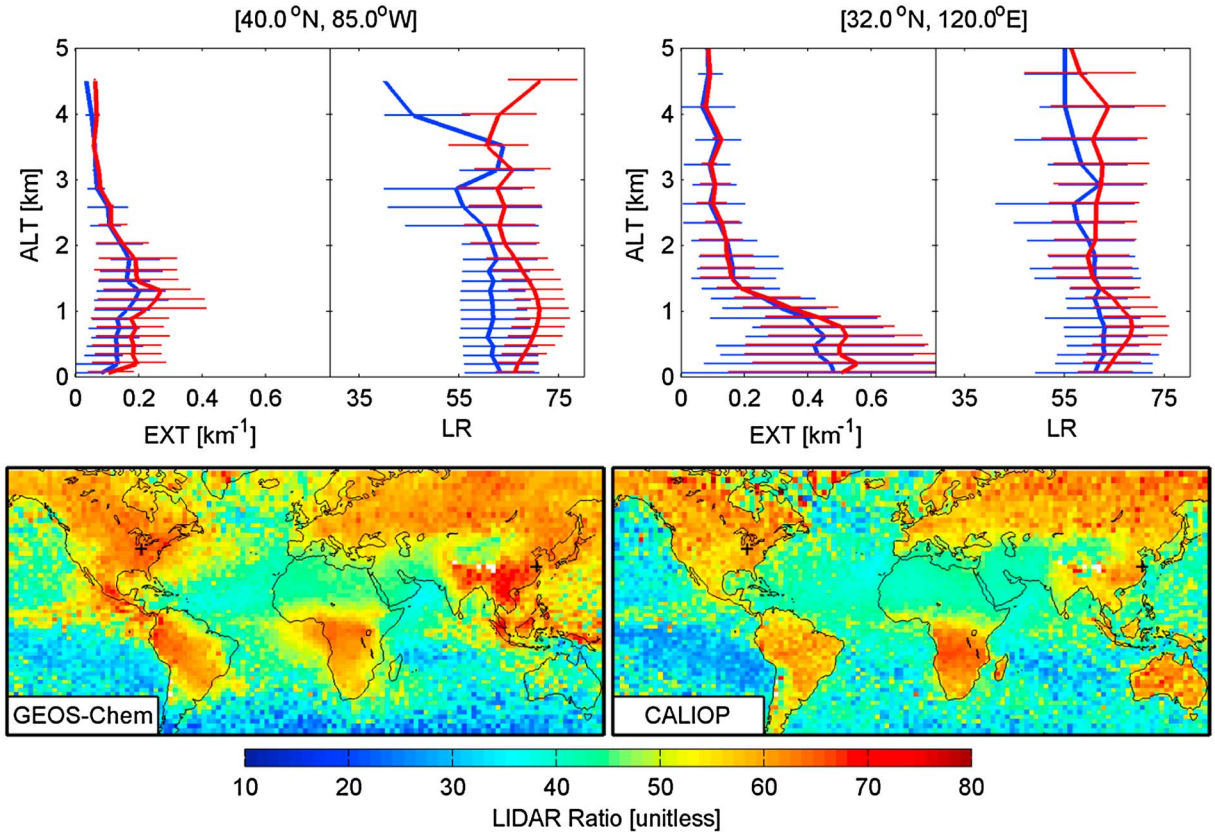

Figure 6. Effect of lidar ratio on CALIOP retrieval for June, July, and August 2006–2011. The upper plots show the extinction coefficient (EXT) and lidar ratio (LR) profiles of the (blue) original CALIOP retrieval and (red) simulation-consistent values, corresponding to the crosshair locations shown in the lower panel. Horizontal lines indicate one standard deviation. The lower row shows vertical extinction-weighted averaged, coincident lidar ratios (top) from GEOS-Chem optical properties and (bottom) from the CALIOP retrieval for the same time period.

determined with Mie calculations [*de Rooij and van der Stap*, 1984; *Mishchenko et al.*, 1999] based on the optical properties used in our GEOS-Chem simulation as a function of relative humidity and species. The lidar ratio for ammonium sulphate increases by 50% from dry conditions (RH = 50%) to moist conditions (RH = 95%). The Mie lidar ratio for dust is not used due to non-sphericity. Table 3 gives the lidar ratios used by the CALIOP retrieval. Direct comparison of species-specific lidar ratios is inhibited by aerosol classifications that are unique to each source. Nonetheless, the values used by GEOS-Chem at mid-level relative humidity are broadly consistent with those from the CALIOP retrieval. Lidar ratios from both the CALIOP retrieval and the GEOS-Chem simulation are about 3–4 times larger for polluted continental (ammonium sulphate and organic carbon) than for clean marine (sea salt). Simulated values, however, indicate variation with relative humidity that could lead to significant differences in S_p under atmospheric conditions.

[46] Figure 6 compares the coincidently sampled lidar ratios from CALIOP with those based upon GEOS-Chem speciation for June, July, and August 2006–2011. A lidar ratio of 40 is used for simulated dust as in the CALIOP retrieval. Retrieval and simulation features are similar; however, simulated lidar ratios are 10–20% higher in polluted regions such as eastern North America, which may arise from elevated regional relative humidity. The impact of these lidar ratio differences must be accounted for during evaluation of the simulated profile.

[47] Equation 2.1 of Part 4 of the CALIOP Algorithm Theoretical Basis Document [*Young et al.*, 2008] gives the lidar equation as:

$$P(r) = \frac{1}{r^2} E_0 \xi [\beta_M(r) + \beta_P(r)] T_M^2(0,r) T_{O_3}^2(0,r) T_P^2(0,r) \quad (7)$$

where

[48] 1. $P(r)$ is the detected backscattered signal from range r from the lidar;

[49] 2. E_0 is the average laser energy for the single shot or composite profile;

[50] 3. ξ is the lidar system parameter;

[51] 4. β_M and β_P are the molecular and particulate volume backscatter coefficients;

[52] 5. T_M^2, $T_{O_3}^2$, and T_P^2 are the two-way molecular, ozone, and particulate transmittances.

[53] A change in the lidar ratio to a new value, $S_P^{'}$, will impact both the particulate volume backscatter coefficient, $\beta_P^{'}$, and particulate transmittance, $T_P^{'}$:

$$P(r) = \frac{1}{r^2} E_0 \xi \left[\beta_M(r) + \beta_P^{'}(r)\right] T_M^2(0,r) T_{O_3}^2(0,r) T_P^{'2}(0,r) \quad (8)$$

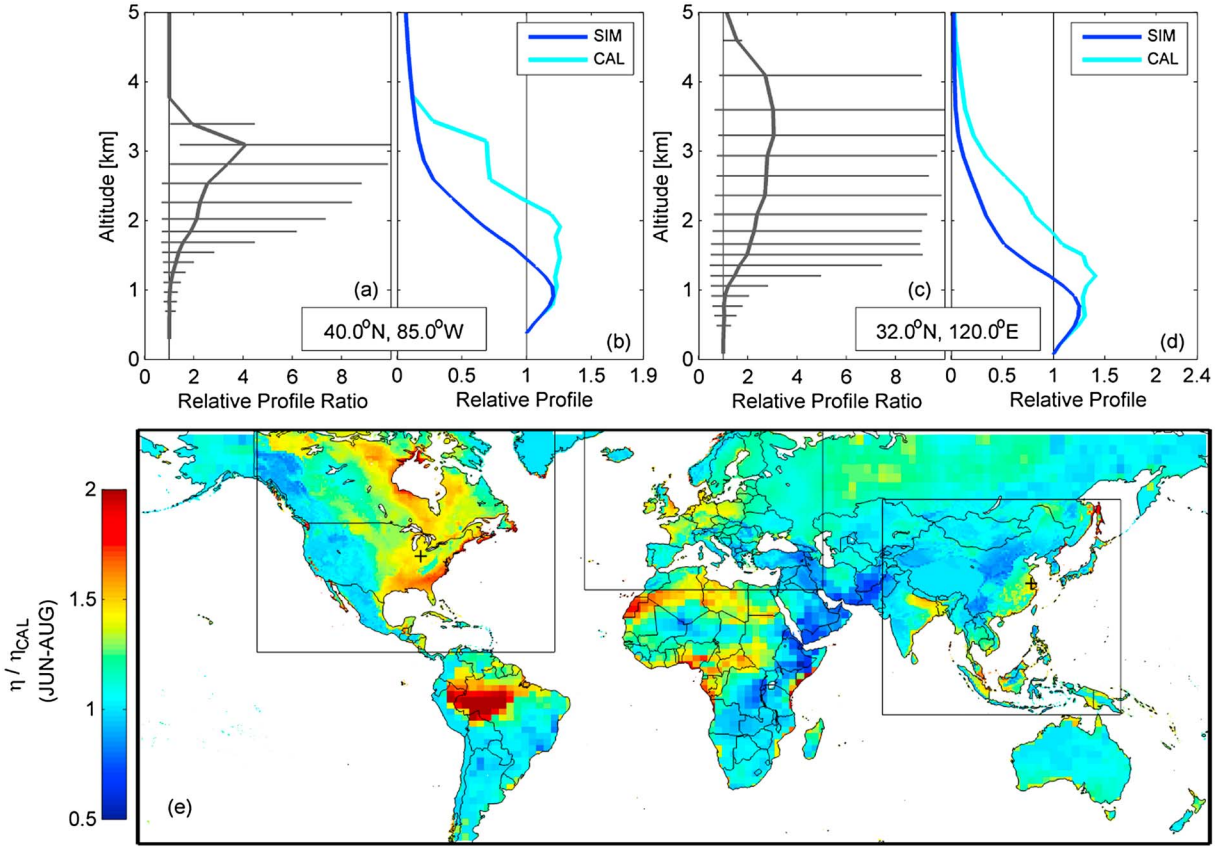

Figure 7. Comparison of simulated (SIM) and CALIOP (CAL) relative-to-surface extinction profiles for June–August. Figures 7a and 7c show the ratio of mean coincidently sampled relative CALIOP and simulated extinction profiles for 2006–2011, normalized to a value of 1 at the surface (dark grey line). Horizontal lines contain one standard deviation of the averaged ratios. Figures 7b and 7d show the mean simulated relative profiles for 2004–2006 at two locations identified by the crosshairs in Figure 7e. Figure 7e shows the global impact of this adjustment on the relationship between AOD at 550 nm and $PM_{2.5}$ (η). Boxes denote nested simulated regions.

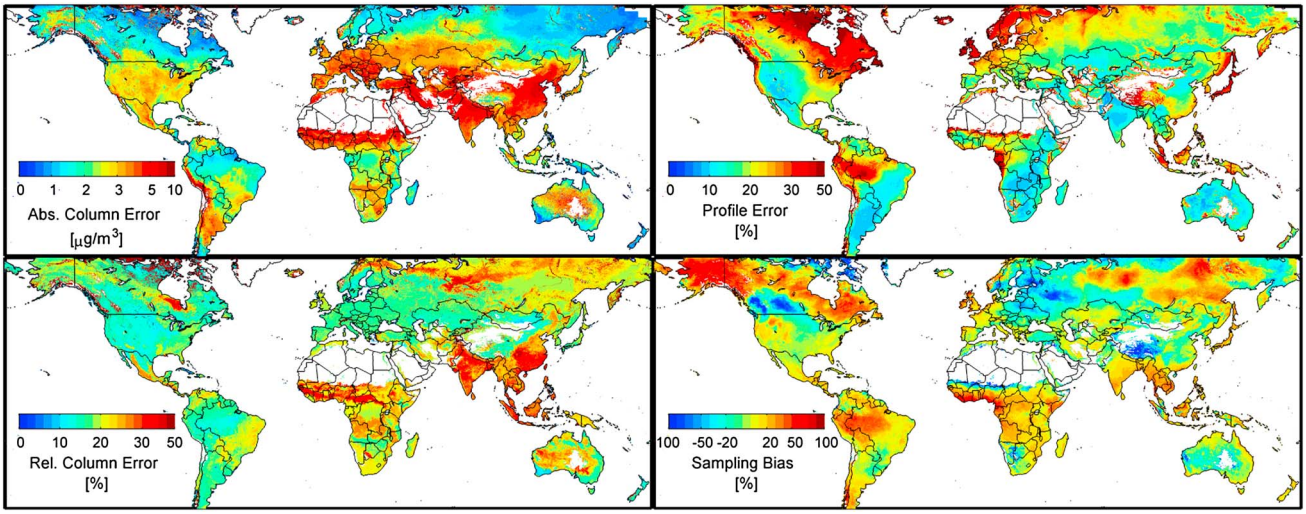

Figure 8. Source-specific error estimate in annual mean $PM_{2.5}$ at a relative humidity of 50%. Error in the aerosol column (AOD) is represented as the sum of absolute and relative terms.

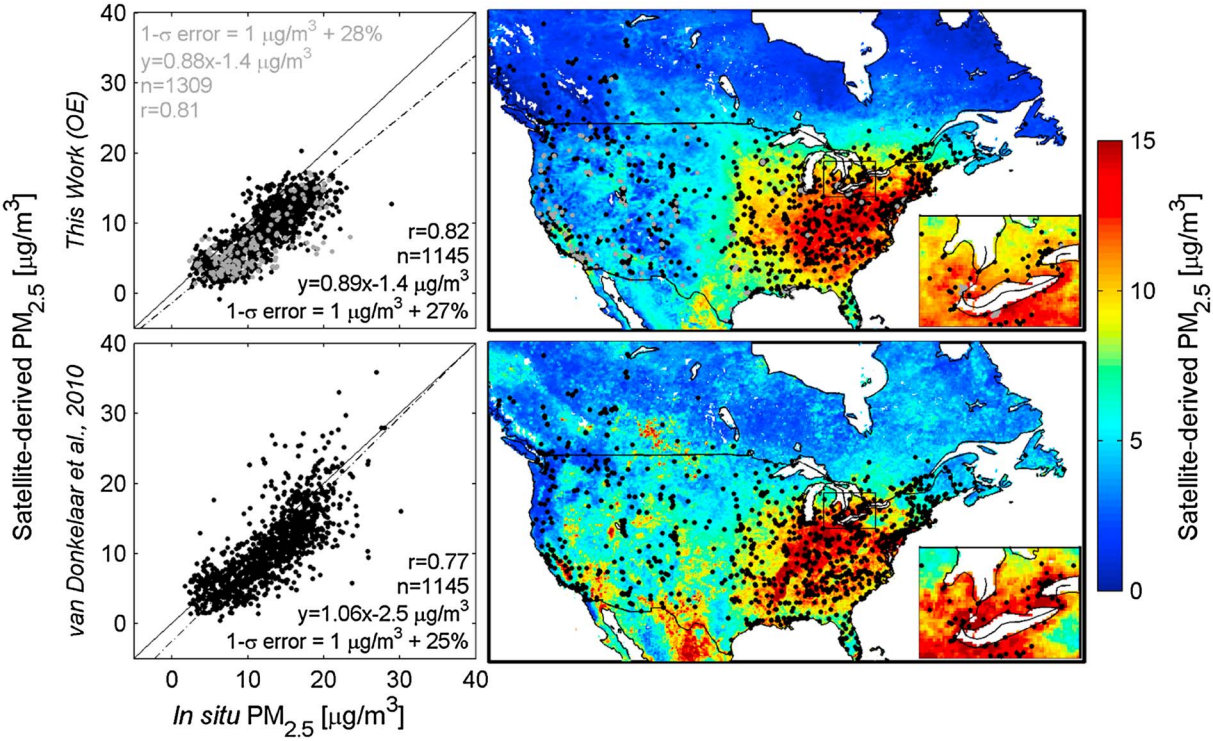

Figure 9. Comparison of satellite-derived OE $PM_{2.5}$ from this work with the previous estimates from *van Donkelaar et al*. [2010] for 2005. The left panels show coincidently sampled averages at locations with at least 10 coincident in situ satellite-derived $PM_{2.5}$ pairs. The right panels show average satellite-derived $PM_{2.5}$. Boxed regions are enlarged within the subpanel plots. Black dots indicate stations included in both scatterplots, and black text provides statistics based upon these locations alone. Grey dots indicate those additional stations that also meet minimum comparison criteria for the OE estimates. Grey text provides statistics based upon all stations available to the OE estimates. $PM_{2.5}$ estimates are at 35% relative humidity.

[54] Dividing (7) by (8), and substituting $T_P^2(0,r) = \exp\left[-2\alpha(r)\tau_p(0,r)\right]$, where $\alpha(r)$ is the multiple scattering factor and $\tau_p(0,r)$ is the particulate optical depth, gives

$$1 = \frac{[\beta_M(r) + \beta_P(r)]\exp\left[-2\alpha(r)\tau_p(0,r)\right]}{\left[\beta_M(r) + \beta_P^{'}(r)\right]\exp\left[-2\alpha^{'}(r)\tau_p^{'}(0,r)\right]} \quad (9)$$

[55] Substituting the lidar ratio,

$$S_p = \frac{\sigma_p}{\beta_p} \quad (10)$$

where σ_p is the particulate volume extinction coefficient, and solving with $\alpha(r)$ and $\alpha^{'}(r)$ treated as unity by assuming thick aerosol layers [*Young et al*., 2008], gives

$$1 = \frac{[\beta_M(r) + \beta_P(r)]}{\left[\beta_M(r) + \beta_P^{'}(r)\right]}\exp\left[2\int_0^r \left(S_P^{'}(r)\beta_P^{'}(r) - S_P(r)\beta_P(r)\right)\mathrm{d}r\right] \quad (11)$$

[56] The extinction coefficients in the top panels of Figure 6 show the effect of iteratively solving equation (11) for $\beta_P^{'}$ from the top of the atmosphere using simulation-consistent values for $S_P^{'}$, and CALIOP v3-01 retrieval values for S_P and β_P for June, July, and August 2006–2011. The effect is cumulative, with increasing impact on approach to the surface and indicates an effect on the relative profile used when relating AOD to $PM_{2.5}$.

[57] Figure 7 further examines the effect of using the CALIOP observations to inform the AOD to $PM_{2.5}$ calculation. Figures 7a and 7c show the ratio of the average relative extinction profile from CALIOP to the simulated aerosol extinction using consistent lidar ratios, for June to August of 2006 to 2011, for the two locations indicated. Figures 7b and 7d show the relative simulated profile and the effect of imposing the CALIOP-to-simulation ratio. The selected locations over eastern North America and eastern China have noteworthy deviations from modeled peak elevation and relative magnitude. *Ford and Heald* [2013] similarly found that GEOS-Chem underestimates aerosol in the lower free troposphere of the southeast United States.

[58] Figure 7e shows the impact of the CALIOP-based profile on the relation between AOD and $PM_{2.5}$, (where $\eta \equiv PM_{2.5}/AOD$). The ratio of the simulated η to the CALIOP-adjusted value, η_{CAL}, suggests profile-related errors are often less than 25%, but in some locations can approach a factor of 2. We therefore scale the simulated aerosol profile according to a monthly, 3 month running mean, CALIOP-based climatology. We multiply each simulated level by the ratio of its mean normalized extinction profile to that retrieved by CALIOP and subsequently scale the adjusted aerosol column to maintain the original simulated total mass. The adjustment is smoothed by averaging neighboring cells thereby reducing noise and

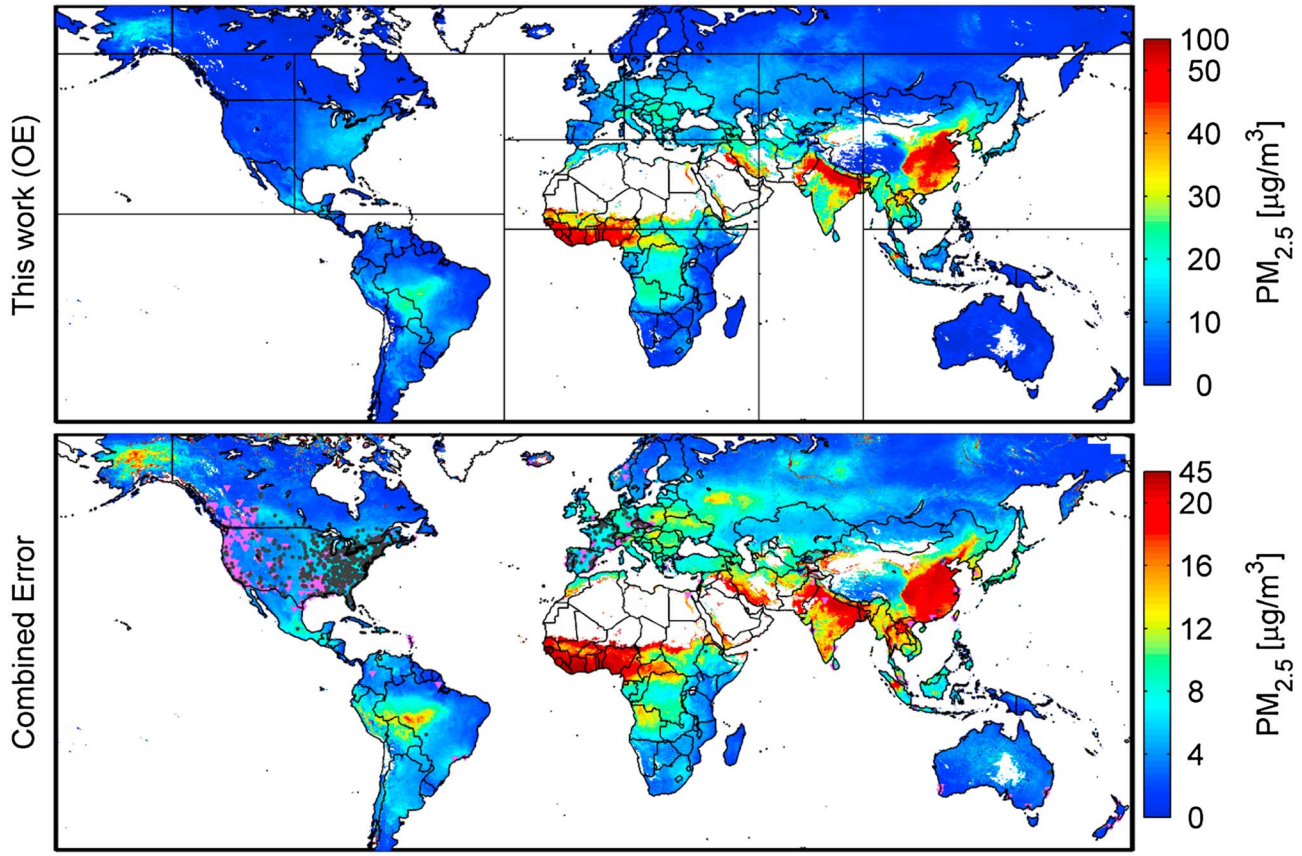

Figure 10. (upper panel) Global OE $PM_{2.5}$ map and (lower panel) combined error at 50% relative humidity for 2005. Markers denote locations of in situ monitors used for validation and indicate whether the location is within (●), biased high above (▲) or biased low beneath (▼) the predicted error. Boxes denote designated regions of Table 4.

providing continuous global coverage. This corrected profile is used to infer $PM_{2.5}$ from AOD.

5. $PM_{2.5}$: Estimation of Errors and Validation With In Situ Data

[59] Three of the major error sources for annual mean satellite-derived $PM_{2.5}$ estimates are AOD accuracy, relative aerosol profile accuracy, and the impact of discontinuous sampling. We estimate AOD error as the sum of an absolute and relative term that contains one standard deviation of the differences between coincidently sampled AERONET and OE AOD over each land type. We extend globally these error estimates from individual stations using land-type percentage cover following the method in section 3.1 used for surface reflectance relationships and observational error. We apply

Table 4. Regional Statistics of $PM_{2.5}$ Concentrations at 50% Relative Humidity

	Statistics (µg/m^3)			Population-Weighted Statistics (µg/m^3)		
Region	Mean	SD[b]	N[c]	Mean	SD[b]	N[c]
World	10.7	12.3	104	27.8	20.5	159
Eastern North America	7.0	4.3	123	11.2	3.3	160
Western North America	3.9	2.7	138	6.5	3.5	203
South America	8.2	5.9	145	7.1	4.2	141
North Africa	27.5	15.3	50	27.4	14.0	162
South Africa	16.4	15.6	172	22.9	21.8	166
Eastern Asia	17.1	16.8	96	37.9	19.9	140
Central Asia	17.8	15.0	107	38.9	19.5	208
South Asia/Australia	3.8	5.1	131	10.9	6.7	127
Eastern Europe	13.5	4.4	121	15.3	4.2	131
Western Europe	10.0	3.6	118	12.0	3.9	108
High North	3.5	3.0	47	4.2	1.8	63

[a]Regions are defined in Figure 10.
[b]Standard deviation.
[c]Average number of daily values for a 0.1° × 0.1° grid with the region for 2005.

our simulated AOD-$PM_{2.5}$ relationship to relate error in AOD to that in $PM_{2.5}$. We represent error in the relative profile by the standard deviation of the relative ratio in between CALIOP and GEOS-Chem (as shown in the profile comparisons of Figure 7) divided by the square root of number of values from MODIS. The relative effect of sampling is approximated using the ratio of coincidently sampled and full annual mean simulated $PM_{2.5}$ values.

[60] Figure 8 shows each of these error sources. AOD column error has the largest impact over parts of Asia, although South America and Africa also show large regional errors. Profile errors are typically less than 20%; however, enhanced profile error is found in regions affected by major biomass burning events, such as central Africa and Brazil, reflecting the uncertainties in smoke injection height. Parts of Canada and northern Europe also show larger profile errors, possibly due to a combined effect of limited sampling with seasonal profile variation. Profile error over northern India is predicted to be relatively low (<15%) despite an adjustment of nearly 50% (shown in Figure 7), due to low variability in the difference between the CALIOP and simulated relative extinction profile. Sampling bias is typically less than 20%, with the exception of some desert, boreal, and biomass burning-affected regions, where biases can exceed 50%.

[61] Figure 9 compares the performance of our OE-based $PM_{2.5}$ values with those of *van Donkelaar et al*. [2010] for 2005 over North America. Our OE algorithm improves coverage (1309 stations versus 1145 stations) and correlation (0.82 versus 0.77) as compared with the earlier work. Error is similar for both data sets ($(1\ \mu g/m^3 + 27\%)$ versus $(1\ \mu g/m^3 + 25\%)$), while slope is slightly degraded (0.89 versus 1.06). $PM_{2.5}$ artifacts in southwestern Canada are reduced compared to previous estimates, due to regionally brighter surface reflectance and increased sampling. The extent of local $PM_{2.5}$ enhancements around urban locations is diminished, as is seen in Figure 9 insets. These effects likely result from a combination of less summer-dominated sampling and improved representation of the urban surface reflectance used in the AOD retrieval. Overcompensation for urban, and other, bright surfaces in the OE AOD is possible due to the removal of the brightest 50% of TOA reflectances used from the MOD/MYD04 algorithm. This would be consistent with the overall underestimate of OE $PM_{2.5}$ as compared to in situ values.

[62] Figure 10 (upper panel) shows our global OE $PM_{2.5}$ estimates at 50% relative humidity. Peak concentrations are approximately $90\ \mu g/m^3$ over eastern China and $80\ \mu g/m^3$ over northern India. High $PM_{2.5}$ concentrations are found in regions heavily influenced by desert dust and seasonal biomass burning.

[63] Figure 10 (lower panel) shows total predicted error, calculated by combining in quadrature the error components from Figure 8. The average predicted error at monitor locations in North America at 35% relative humidity (RH) is $(2.5\ \mu g/m^3 + 31\%)$, which exceeds the observed 1-σ error level of $\pm(1.0\ \mu g/m^3 + 28\%)$. The predicted 1-$\sigma$ error contains 75% of the differences with in situ monitors and implies that the true error is slightly lower. The majority of sites with errors that exceed our predicted estimates are in the western half of the continent, suggesting that for some regions, such as the San Joaquin Valley in California, USA, the higher satellite-derived $PM_{2.5}$ values estimated in the previous work better characterize local concentrations than our present OE values. Error estimates at European monitoring sites perform similarly to North America, with 74% of the OE values within the mean co-located 50% RH error estimate of $(3.5\ \mu g/m^3 + 30\%)$. Error outside Canada, USA, and Europe appears to be underestimated, however, with only 40% of differences falling within the mean 50% RH co-located error of $\pm(3.0\ \mu g/m^3 + 35\%)$. It is unclear whether this lower accuracy in error prediction reflects a decrease in representativity of the available in situ data due to variability within the pixel's approximately $10\ km \times 10\ km$ [e.g., *Brauer*, 2010; *Lindén et al*., 2012] or a decrease in the quality of the OE error estimates.

[64] Table 4 provides regional statistics of $PM_{2.5}$ at 50% RH, as well as sampling. Population-weighted $PM_{2.5}$ exceeds unweighted spatial averages for all regions except South America and North Africa, where enhancements due to biomass burning and Saharan dust dominate. A global population-weighted mean $PM_{2.5}$ for 2005 of $27.8\ \mu g/m^3$ is estimated, with population-weighted regional values reaching nearly $40\ \mu g/m^3$ over Eastern and Central Asia.

6. Conclusions

[65] We develop an optimal estimation (OE) based approach to global $PM_{2.5}$ estimation that combines satellite observations of top-of-atmosphere (TOA) reflectance from the MODIS instrument with prior $PM_{2.5}$ concentrations from the GEOS-Chem chemical transport model. Simulated TOA reflectances and associated AOD Jacobians are calculated with the LIDORT radiative transfer model. Surface reflectance relationships are indexed by land type. Error estimates of both simulated and observed values needed for OE calculations are determined by comparison with AERONET measurements of AOD. These error estimates are extended globally using cross correlation and speciation for GEOS-Chem error and land type coverage for satellite-based observational error. Final OE-based AOD values generally perform as well as, or better than, either simulated or satellite-retrieval values alone. India and East Asia are exceptions. Regional daily comparisons with coincident AERONET measurements yield slopes of 0.7–1.1 and correlations of 0.67–0.89.

[66] We evaluate and improve the GEOS-Chem AOD to $PM_{2.5}$ relationship by comparing simulated relative extinction profiles with those retrieved by the CALIOP space-borne lidar. The comparison used consistent optical properties for the CALIOP retrieval and GEOS-Chem. The simulated and measured profiles often agree to within 25%; however, differences vary by up to a factor of 2 in some regions. We therefore incorporate a monthly, 3 month running mean, adjustment to the GEOS-Chem profile to match CALIOP mean values.

[67] We predict the error of our final OE $PM_{2.5}$ estimates based upon uncertainties in the sampling, the relative extinction profile, and the AOD itself. Our predicted error estimates capture at least 68% of values over Canada, USA, and Europe when compared with available in situ $PM_{2.5}$ monitors. The accuracy of the error is less clear outside of these locations, likely due to a combination of decreased representativity of the in situ data itself and increased uncertainty in the OE error values.

[68] We find good agreement between our OE $PM_{2.5}$ values over North America (slope = 0.89; $r = 0.82$), with increased coverage and correlation relative to earlier work. We find observationally a 1-σ error of $\pm(1\,\mu g/m^3 + 28\%)$, which implies that our predicted error of $\pm(2.5\,\mu g/m^3 + 31\%)$ is slightly overestimated over this region as a whole. Subregions, such as the western United States, can contain clusters of sites with error beyond the estimated range, and whose measured values are closer to those estimated in previous work [e.g., *van Donkelaar et al*., 2010]. Overall, OE agreement is comparable to the previous work, with OE providing improved sampling (1309 sites versus 1145 sites) and correlation (0.82 versus 0.77), but lower slope (0.89 versus 1.06) and similar error ($1\,\mu g/m^3 + 27\%$ versus $1\,\mu g/m^3 + 25\%$). Global population-weighted $PM_{2.5}$ at 50% RH is estimated as $27.8\,\mu g/m^3$.

[69] OE provides a framework within which improvements to both simulated and retrieved aerosol can be incorporated. A greater understanding of the magnitude and impact of error sources will lead to improved estimates. Specific future work should develop the aerosol simulation to reduce the bias in the extinction vertical profile. Additional in situ $PM_{2.5}$ monitors outside of Canada, the United States, and Europe would provide valuable information for global comparisons. Collocation of AOD and $PM_{2.5}$ measurements (e.g., www.spartan-network.org) would characterize errors in simulating that quantity. Incorporation of additional wavelengths into the OE framework, such as those deployed by the MODIS Deep Blue retrieval [*Hsu et al*., 2006], could improve aerosol estimates over bright surfaces.

[70] **Acknowledgments.** We are grateful to the CALIOP, AERONET, NAPS, and AQS teams for making available data used here. This work was funded by Health Canada and the Natural Sciences and Engineering Research Council of Canada.

References

Alexander, B., R. J. Park, D. J. Jacob, Q. B. Li, R. M. Yantosca, J. Savarino, C. C. W. Lee, and M. H. Thiemens (2005), Sulfate formation in sea-salt aerosols: Constraints from oxygen isotopes, *J. Geophys. Res.*, *110*, D10307, doi:10.1029/2004JD005659.

Anderson, H. R., et al. (2012), Satellite-based estimates of ambient air pollution and global variations in childhood asthma prevalence, *Environ. Health Perspect.*, *120*(9), 1333–1339.

Bowman, K. W., et al. (2006), Tropospheric emission spectrometer: Retrieval method and error analysis, *IEEE Trans. Geosci. Remote Sens.*, *44*(5), 1297–1307.

Brauer, M. (2010), How much, how long, what, and where: Air pollution exposure assessment for epidemiologic studies of respiratory disease, *Proc. Am. Thorac. Soc.*, *7*, 111–115.

Chen, D., X. T. Wang, M. B. McElroy, K. He, R. M. Yantosca, and P. LeSager (2009), Regional CO pollution in China simulated by the high-resolution nested-grid GEOS-Chem model, *Atmos. Chem. Phys.*, *9*, 3825–3839.

Crouse, D. L., et al. (2012), Risk of nonaccidental and cardiovascular mortality in relation to long-term exposure to low concentrations of fine particulate matter: A Canadian national-level cohort study, *Environ. Health Perspect.*, *120*(5), 708–714.

de Almeida Castanho, A. D., R. Prinn, V. Martins, M. Herold, C. Ichoku, and L. T. Molina (2007), Analysis of Visible/SWIR surface reflectance ratios for aerosol retrievals from satellite in Mexico City urban area, *Atmos. Chem. Phys.*, *7*, 5467–5477.

de Rooij, W. A., and C. C. A. H. van der Stap (1984), Expansion of Mie scattering matrices in generalized spherical functions, *Astron. Astrophys.*, *131*, 237–248.

Diner, D. J., et al. (1998), Multi-angle Imaging SpectroRadiometer (MISR) instrument description and experiment overview, *IEEE Trans. Geosci. Remote Sens.*, *36*(4), 1072–1087.

Dockery, D. W., C. A. Pope, X. P. Xu, J. D. Spengler, J. H. Ware, M. E. Fay, B. G. Ferris Jr, and F. E. Speizer (1993), An association between air-pollution and mortality in six United-States cities, *N. Engl. J. Med.*, *329*(24), 1753–1759.

Drury, E., D. J. Jacob, J. Wang, R. J. D. Spurr, and K. Chance (2008), Improved algorithm for MODIS satellite retrievals of aerosol optical depths over western North America, *J. Geophys. Res.*, *113*, D16204, doi:10.1029/2007JD009573.

Drury, E., et al. (2010), Synthesis of satellite (MODIS), aircraft (ICARTT), and surface (IMPROVE, EPA-AQS, AERONET) aerosol observations over eastern North America to improve MODIS aerosol retrievals and constrain surface aerosol concentrations and sources, *J. Geophys. Res.*, *115*, D14204, doi:10.1029/2009JD012629.

Dubovik, O., M. Herman, A. Holdak, T. Lapyonok, D. Tanré, J. L. Deuzé, F. Ducos, A. Sinyuk, and A. Lopatin (2011), Statistically optimized inversion algorithm for enhanced retrieval of aerosol properties from spectral multi-angle polarimetric satellite observations, *Atmos. Meas. Tech.*, *4*, 975–1018.

Evans, M. J., and D. J. Jacob (2005), Impact of new laboratory studies of N2O5 hydrolysis on global model budgets of tropospheric nitrogen oxides, ozone, and OH, *Geophys. Res. Lett.*, *32*, L09813, doi:10.1029/2005GL022469.

Fairlie, T. D., D. J. Jacob, and R. J. Park (2007), The impact of transpacific transport of mineral dust in the United States, *Atmos. Environ.*, *41*(6), 1251–1266.

Ford, B., and C. L. Heald (2012), An A-train and model perspective on the vertical distribution of aerosols and CO in the Northern Hemisphere, *J. Geophys. Res.*, *117*, D06211, doi:10.1029/2011JD016977.

Ford, B., and C. L. Heald (2013), Aerosol loading in the Southeastern United States: Reconciling surface and satellite observations, *Atmos. Chem. Phys. Discuss.*, *13*, 9917–9952.

Freidl, M. A., D. Sulla-Menashe, B. Tan, A. Schneider, N. Ramankutty, A. Sibley, and X. Huang (2010), MODIS Collection 5 global land cover: Algorithm refinements and characterization of new datasets, *Remote Sens. Environ.*, *114*, 168–182.

Hasekamp, O. P., and J. Landgraf (2005), Linearization of vector radiative transfer with respect to aerosol properties and its use in satellite remote sensing, *J. Geophys. Res.*, *110*, D04203, doi:10.1029/2004JD005260.

Henze, D. K., J. H. Seinfeld, N. L. Ng, J. H. Kroll, T. M. Fu, D. J. Jacob, and C. L. Heald (2008), Global modeling of secondary organic aerosol formation from aromatic hydrocarbons: High- vs. low-yield pathways, *Atmos. Chem. Phys.*, *8*, 2405–2421.

Holben, B. N., et al. (1998), AERONET - A federated instrument network and data archive for aerosol characterization, *Remote Sens. Environ.*, *66*(1), 1–16.

Holben, B. N., et al. (2001), An emerging ground-based aerosol climatology: Aerosol optical depth from AERONET, *J. Geophys. Res.*, *106*(D11), 12067–12097.

Hsu, N. C., S. C. Tsay, M. D. King, and J. R. Herman (2006), Deep blue retrievals of Asian aerosol properties during ACE-Asia, *Ieee Trans. Geosci. Remote Sens.*, *44*(11), 3180–3195.

Jacob, D. J. (2000), Heterogeneous chemistry and tropospheric ozone, *Atmos. Environ.*, *34*(12–14), 2131–2159.

Kahn, R. A., D. Nelson, M. Garay, R. Levy, M. Bull, D. Diner, J. Martonchik, S. Paradise, E. Hansen, and L. Remer (2009), MISR aerosol product attributes, and statistical comparisons with MODIS, *Trans. Geosci. Remote Sens.*, *47*(12), 4095–4114.

Kloog, I., P. Koutrakis, B. A. Coull, H. J. Lee, and J. Schwartz (2011), Assessing temporally and spatially resolved PM2.5 exposures for epidemiological studies using satellite aerosol optical depth measurements, *Atmos. Environ.*, *45*, 6267–6275.

Kuhns, H., E. M. Knipping, and J. M. Vukovich (2005), Development of a United States-Mexico emissions inventory for the Big Bend Regional Aerosol and Visibility Observational (BRAVO) Study, *J. Air Waste Manage. Assoc.*, *55*(5), 677–692.

Lee, C., R. V. Martin, A. van Donkelaar, G. O'Byrne, N. Krotkov, A. Richter, L. G. Huey, and J. S. Holloway (2009), Retrieval of vertical columns of sulfur dioxide from SCIAMACHY and OMI: Air mass factor algorithm development, validation, and error analysis, *J. Geophys. Res.*, *114*, D22303, doi:10.1029/2009JD012123.

Levy, R. C., L. A. Remer, and O. Dubovik (2007a), Global aerosol optical properties and application to Moderate Resolution Imaging Spectroradiometer aerosol retrieval over land, *J. Geophys. Res.*, *112*, D13210, doi:10.1029/2006JD007815.

Levy, R. C., L. A. Remer, S. Mattoo, E. F. Vermote, and Y. J. Kaufman (2007b), Second-generation operational algorithm: Retrieval of aerosol properties over land from inversion of Moderate Resolution Imaging Spectroradiometer spectral reflectance, *J. Geophys. Res.*, *112*, D13211, doi:10.1029/2006JD007811.

Levy, R. C., L. A. Remer, R. G. Kleidman, S. Mattoo, C. Ichoku, R. Kahn, and T. F. Eck (2010), Global Evaluation of the Collection 5 MODIS dark-target aerosol product over land, *Atmos. Chem. Phys.*, *10*, 10399–10420.

Levy, R. C., S. Mattoo, L. A. Munchak, L. A. Remer, A. M. Sayer, and N. C. Hsu (2013), The Collection 6 MODIS aerosol products over land and ocean, *Atmos. Meas. Tech. Discuss.*, *6*, 159–259.

Lim, S. S., et al. (2012), A comparative risk assessment of burden of disease and injury attributable to 67 risk factors and risk factor clusters in 21 regions, 1990–2010: A systematic analysis for the Global Burden of Disease Study 2010, *Lancet*, *380*, 2224–2260.

Lindén, J., J. Bomanb, B. Holmera, S. Thorssona, and I. Eliassonc (2012), Intra-urban air pollution in a rapidly growing Sahelian city, *Environ. Int.*, *40*, 51–62.

Liu, Y., R. J. Park, D. J. Jacob, Q. B. Li, V. Kilaru, and J. A. Sarnat (2004), Mapping annual mean ground-level PM2.5 concentrations using Multiangle Imaging Spectroradiometer aerosol optical thickness over the contiguous United States, *J. Geophys. Res.*, *109*, D22206, doi:10.1029/2004JD005025.

Lucht, W., C. B. Schaaf, and A. H. Strahler (2000), An algorithm for the retrieval of albedo from space using semiempirical BRDF models, *Ieee Trans. Geosci. Remote Sens.*, *38*(2), 977–998.

Martin, R. V., D. J. Jacob, K. Chance, T. P. Kurosu, P. I. Palmer, and M. J. Evans (2003a), Global inventory of nitrogen oxide emissions constrained by space-based observations of NO2 columns, *J. Geophys. Res.*, *108*(D17), 4537, doi:10.1029/2003JD003453.

Martin, R. V., D. J. Jacob, R. M. Yantosca, M. Chin, and P. Ginoux (2003b), Global and regional decreases in tropospheric oxidants from photochemical effects of aerosols, *J. Geophys. Res.*, *108*(D3), 4097, doi:10.1029/2002JD002622.

Mishchenko, M. I., J. M. Dlugach, E. G. Yanovitskij, and N. T. Zakharova (1999), Bidirectional reflectance of flat optically thick particulate layers: An efficient radiative transfer solution and applications to snow and soil surfaces, *J. Quant. Spectrosc. Radiat. Transfer*, *63*, 409–432.

Nassar, R., J. A. Logon, I. A. Megretskaia, L. T. Murray, L. Zhang, and D. B. A. Jones (2009), Analysis of tropical tropospheric ozone, carbon monoxide and water vapor during the 2006 El Niño using TES observations and the GEOS-Chem model, *J. Geophys. Res.*, vol. *114*, D17304, *in press*.

Olivier, J. G. J., J. J. M. Berdowski, J. A. H. W. Peters, J. Bakker, A. J. H. Visschedijk, and J. J. Bloos (2002), Applications of EDGAR Including a description of EDGAR 3.2 reference database with trend data for 1970–1995, *Document*.

Omar, A., et al. (2009), The CALIPSO automated aerosol classification and lidar ratio selection algorithm, *J. Atmos. Oceanic Tech.*, *26*, 1994–2014.

Park, R. J., D. J. Jacob, M. Chin, and R. V. Martin (2003), Sources of carbonaceous aerosols over the United States and implications for natural visibility, *J. Geophys. Res.*, *108*(D12), 4355, doi:10.1029/2002JD003190.

Park, R. J., D. J. Jacob, B. D. Field, R. M. Yantosca, and M. Chin (2004), Natural and transboundary pollution influences on sulfate-nitrate-ammonium aerosols in the United States: Implications for policy, *J. Geophys. Res.*, *109*, D15204, doi:10.1029/2003JD004473.

Pope, C. A., M. Ezzati, and D. W. Dockery (2009), Fine-particulate air pollution and life expectancy in the United States, *N. Engl. J. Med.*, *360*, 376–386.

Pye, H. O. T., H. Liao, S. Wu, L. J. Mickley, D. J. Jacob, D. K. Henze, and J. H. Seinfeld (2009), Effect of changes in climate and emissions on future sulfate-nitrate-ammonium aerosol levels in the United States, *J. Geophys. Res.*, *114*, D01205, doi:10.1029/2008JD010701.

Remer, L. A., et al. (2005), The MODIS aerosol algorithm, products, and validation, *J. Atmos. Sci.*, *62*(4), 947–973.

Remer, L. A., S. Mattoo, R. C. Levy, and L. A. Munchak (2013), MODIS 3 km aerosol product: Algorithm and global perspective, *Atmos. Meas. Tech. Discuss.*, *6*, 69–112.

Rodgers, C. D. (2000), *Inverse Methods for Atmospheric Sounding: Theory and Practice*, World Scientific, Hackensack, NJ, USA pp. 65–74.

Sayer, A. M., G. E. Thomas, R. G. Grainger, E. Carboni, C. Poulsen, and R. Siddans (2012), Use of MODIS-derived surface reflectance data in the ORAC-AATSR aerosol retrieval algorithm: Impact of differences between sensor spectral response functions, *Remote Sens. Environ.*, *116*, 177–188.

Spurr, R. (2008), LIDORT and VLIDORT: Linearized pseudo-spherical scalar and vector discrete ordinate radiative transfer models for use in Remote sensing retrieval problems. *Light Scattering Reviews*, Volume *3*, ed. A. Kokhanovsky, Springer.

Streets, D. G., et al. (2003), An inventory of gaseous and primary aerosol emissions in Asia in the year 2000, *J. Geophys. Res.*, *108*(D21), 8809, doi:10.1029/2002JD003093.

Streets, D. G., Q. Zhang, L. T. Wang, K. B. He, J. M. Hao, Y. Wu, Y. Tang, and G. R. Carmichael (2006), Revisiting China's CO emissions after the Transport and Chemical Evolution over the Pacific (TRACE-P) mission: Synthesis of inventories, atmospheric modeling, and observations, *J. Geophys. Res.*, *111*, D14306, doi:10.1029/2006JD007118.

Thornton, J. A., L. Jaegle, and V. F. McNeill (2008), Assessing known pathways for HO2 loss in aqueous atmospheric aerosols: Regional and global impacts on tropospheric oxidants, *J. Geophys. Res.*, *113*, D05303, doi:10.1029/2007JD009236.

van Donkelaar, A., et al. (2008), Analysis of aircraft and satellite measurements from the Intercontinental Chemical Transport Experiment (INTEX-B) to quantify long-range transport of East Asian sulfur to Canada, *Atmos. Chem. Phys.*, *8*(11), 2999–3014.

van Donkelaar, A., R. V. Martin, M. Brauer, R. Kahn, R. Levy, C. Verduzco, and P. J. Villeneuve (2010), Global estimates of ambient fine particulate matter concentrations from satellite-based aerosol optical depth: Development and application, *Environ. Health Perspect.*, *118*(6), 847–855.

van Donkelaar, A., R. V. Martin, R. C. Levy, M. da Silva, M. Krzyzanowski, N. E. Chubarova, E. Semutnikova, and A. J. Cohen (2011), Satellite-derived estimates of ground-level fine particulate matter during extreme events: A case study of the Moscow fires in 2010, *Atmos. Environ.*, *45*, 6225–6232.

van Donkelaar, A., R. V. Martin, A. N. Pasch, J. J. Szykman, L. Zhang, Y. X. Wan and, D. Chen (2012), Improving the accuracy of daily satellite-derived ground-level fine aerosol concentration estimates for North America, *Environ. Sci. Tech.*, *46*, 11971–11978.

Villeneuve, P. J., M. S. Goldberg, R. T. Burnett, A. van Donkelaar, H. Chen, and R. V. Martin (2011), Associations between cigarette smoking, obesity, sociodemographic characteristics, and remote sensing derived estimates of ambient PM2.5: Results from a Canadian population-based survey, *J. Occup. Environ. Med.*, *68*(12), 920–7.

Wang, J., X. Liu, S. A. Christopher, J. S. Reid, E. Reid, and H. Maring (2003), The effects of non-sphericity on geostationary satellite retrievals of dust aerosols, *Geophys. Res. Lett.*, *30*(24), 2293, doi:10.1029/2003GL018697.

Wang, J., X. G. Xu, R. Spurr, Y. X. Wang, and E. Drury (2010), Improved algorithm for MODIS satellite retrievals of aerosol optical thickness over land in dusty atmosphere: Implications for air quality monitoring in China, *Remote Sens. Environ.*, *114*(11), 2575–2583.

Waquet, F., B. Cairns, K. Knobelspiesse, J. Chowdhary, L. D. Travis, B. Schmid, and M. I. Mishchenko (2009), Polarimetric remote sensing of aerosols over land, *J. Geophys. Res.*, *114*, D01206, doi:10.1029/2008JD010619.

Winker, D. M., M. A. Vaughan, A. Omar, Y. Hu, and K. A. Powell (2009), Overview of the CALIPSO mission and CALIOP data processing algorithms, *J. Atmos. Oceanic Tech.*, *26*, 2310–2323.

Young, S. A., D. M. Winker, M. A. Vaughan, Y. Hu, and R. E. Kuehn (2008), CALIOP algorithm theoretical basis document, Part 4: Extinction retrieval algorithms*Rep*.

Zhang, H., R. M. Hoff, and J. A. Engel-Cox (2009), The relation between Moderate Resolution Imaging Spectroradiometer (MODIS) aerosol optical depth and PM2.5 over the United States: A geographical comparison by EPA regions, *J. Air Waste Manage. Assoc.*, *59*, 1358–1369.